UNIVERSITY
OF TRENTO - Italy
Department of Physics

CONFINDUSTRIA TRENTO

POLO
MECCATRONICA
Impresa Innovazione Formazione

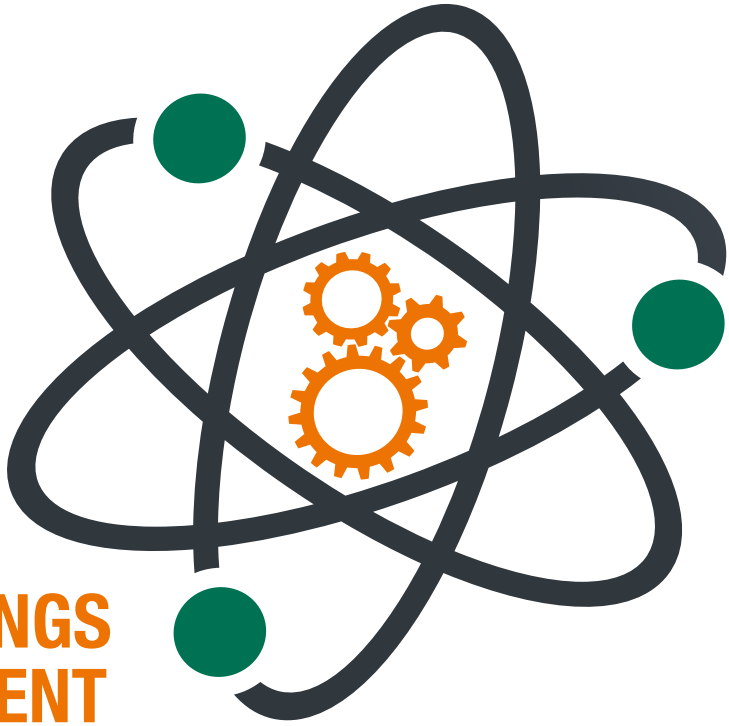

PROCEEDINGS OF THE EVENT

IPSP2015

INDUSTRIAL PROBLEM SOLVING WITH PHYSICS

Trento (Italy)

July 20 – 25, 2015

Proceedings of the event IPSP2015

Industrial Problem Solving with Physics

Trento, July 20 – 25, 2015

Editors
Martino Bernard
Stefano Tondini
Giuliano Zendri

Trento
Università degli Studi di Trento

Proceedings of the event IPSP2015: Industrial Problem Solving with Physics: Trento, July 20 - 25, 2015 / editors Martino Bernard, Stefano Tondini, Giuliano Zendri. - Trento: Università degli Studi di Trento, 2015. - 85 p.: ill. - ISBN: 978-88-8443-674-0.

Document Class available at `https://github.com/mrgrass/IPSP_latex_Class`

PREFACE

Dear reader,
Thank you for your interest in the second edition of "Industrial Problem Solving with Physics". The first edition of IPSP has proven itself as being an effective tool in reaching innovative solutions of interest for industries. The event laid the foundation for a research activity that continued even after the workshop's conclusion.
After the great success of IPSP2014, this second edition has seen an increased interest and a higher number of those attending, both among companies and researchers... the "brains". What's more, the IPSP2015 Scientific Committee has been formed by three Ph.D. Physics students again. As organizers we tried to pursue our goal of bringing academic knowledge into solving business issues with three main steps in mind: to qualify physicists or, more generally, young researchers as regard industrial realities; to give young researchers the opportunity to apply their knowledge and skills in areas out of their own research field; to understand the needs and demands of companies towards the University.
The impact of the results on the local area is crucial because it makes business realities as well as young scientists find favorable conditions for building profitable collaborations. The second edition of IPSP (http://events.unitn.it/en/ipsp2015) has gotten a positive feedback from all participants. Young researchers actively took part in brainstorming and in the technical and scientific activities. On the other hand, the companies were satisfied with the work carried out by research teams, appreciating the variety of suggested approaches to open issues. In particular, the workweek has kicked started a collaboration between the Department of Physics and one of the participating companies for a more detailed analysis of the results obtained during the workshop. A further company claimed it would implement one of the solutions proposed during the brainstorming, in order to carry on an optimization study on a product.
From this it is clear that the format is establishing its function of connecting the high-tech industries of the region Trentino-Alto Adige with the applied research carried out at the University of Trento. The benefit that arises from this cooperation is two-fold. It consists in both pulling down technological barriers, which may limit the competitive development of the local companies, and creating a new type of placement, based on a novel scouting concept for researchers of scientific

training.
The document is structured as follows: after a brief introduction from the Research and Technology Transfer Support Division of the University of Trento, the industrial problems and their solutions are explained in three chapters. The first chapter is about the problem presented by COSTER Tecnologie Speciali S.p.a., the second one is dedicated to the problem of LA SPORTIVA S.p.a., the last one concerns the problem proposed by PAMA S.p.a. Each chapter gives at first the problem overview, then presents the different investigation approaches as well as the results obtained during the IPSP2015 week.

Martino Bernard
Stefano Tondini
Giuliano Zendri
Scientific Commitee of Industrial Problem Solving with Physics 2015

INTRODUCTION

A Knowledge Transfer Approach

Industrial Problem Solving with Physics 2015 (IPSP2015) is a one-week event organized by the Department of Physics, the Doctoral School in Physics and the Research and Technology Transfer Support Division of the University of Trento, in collaboration with Confindustria Trento and Polo Meccatronica - Trentino Sviluppo. The aim of this event is to boost the connection between University and Industry. Young and motivated researchers have the chance to prove their skills, while selected companies can experience the unique opportunity to collaborate with young and talented brains. The second edition of IPSP (year 2015) has taken place from July 20 to July 25, 2015, at the Polo scientifico e tecnologico "Fabio Ferrari" at the University of Trento.
Leading research and academic institutions are increasingly fostering a problem-solving approach that encourages researchers to work together across departments, fields, and institutional boundaries. The resulting collaborations include partnerships with industry and other research institutions. Yet, leading research organisations welcome all industry partners who seek practicable and pragmatic solutions, and who share and celebrate the entrepreneurial spirit. Together, academia and industry can make great progress in creating new knowledge, in shaping new inventions and in increasing the amount of activities in knowledge and technology transfer.
Industrial Problem Solving with Physics has been constructed based on 'Physics with Industry' (PwI) organized in the Netherlands by some leading research institutions. The annual workshop PwI is organized by FOM, Technology Foundation STW, and the Lorentz Center in Leiden. It is intended to encourage cooperation and exchange of knowledge between academia and industry, generating results that are intended to be public. In the stimulating setting of the Lorentz Center, scientists and researchers from both university and industry work closely together during one week to find original solutions to challenging industrial problems. This workshop offers the companies the opportunity to have a dedicated team of highly motivated physicists from universities and research institutes spending a full week tackling the specific industrial problem. The teams consist of PhD students and postdocs, and are led by a number of senior academic scientists. The teams are

composed of physicists with different backgrounds, ensuring the problems are approached from different angles. Researchers from companies are asked to be present and actively participate during the full week, providing the team with relevant input, and ensuring that proposed solutions remain realistic and practically feasible. Since its start in 2010, this annual workshop has proved a very successful project.

The IPSP competition

Industrial Problem Solving with Physics takes its generation on the basis that the collaboration between universities and the industry is increasingly perceived as a vehicle to enhance innovation. In the literature universitiesindustry collaboration refers to the interaction between any parts of the higher educational system and industry aiming mainly to encourage knowledge and technology exchange. Of late, there has been a substantial increase in these collaborations in several nations including: the United States, Japan, Singapore and the European Union Countries. This increase has been attributed to a combination of pressures on both industry and universities. For industry, pressures have included rapid technological change, shorter product life cycles and intense global competition that have radically transformed the current competitive environment for most firms. With regards to universities, pressures have included the growth in new knowledge and the challenge of rising costs and funding problems, which have exerted enormous resource burdens on universities to seek relationships with firms to enable them to remain at the leading edge in all subject areas.
The foundations of IPSP rely on the fact that further understanding the links between university and industry has significant implications for public policy and the rationales beyond funding basic research in universities as well as firms. R&D collaborations based on relationships are the preferred ways of exchange, enabling regular face-to-face contacts, reciprocal and bi-directional knowledge exchanges as well as the circulation of ideas between theory and practice. On these conceptual bases IPSP has been thought and implemented in the first two years. In sum, border-crossing team work and inter-organizational collaboration activities (such as those conducted during IPSP) can be seen as one of the most important mechanisms of knowledge flows from university to industry. This finds further support in the fact that potential tensions and cultural barriers between university and industry due to different institutional norms governing public and private knowledge can be overcome in trust-based interactions where corporate and academic researchers act as boundary spanners (Bruneel et al., 2010). It is particularly the person-to-person interaction that matters in the transfer of highly advanced technological knowledge.

How does IPSP work

Three companies and thirty brains (master course students, PhD students and fellow researchers) are selected and will work together for one week to find solutions to practical industrial problems proposed by the participating companies. Solutions are aimed to be achieved through inspiration, prior art search, resources

and facilities available at the Department of Physics of the University of Trento. IPSP aims at creating a bridge for the transfer of technological knowledge and human resources between the University, in particular the Department of Physics, and companies. Students and researchers participating in the event have the opportunity to tackle new practical challenges, crossing more than one area of their scientific background. Moreover, participants will experience the practice of confidentiality, requested by the enterprises to disclose internal information, and learn the basics of patentability of inventions.
At the same time, companies can obtain a solution to their problems and experience an alternative approach about how to reach their goals. Thanks to a continuous dialogue with the team, R&D industry managers can have the chance to scout young and talented people for future collaborations. Problems not fully solved in the one week IPSP format are the starting point of research contracts or projects.
At the end of the week the solutions will be evaluated by a scientific committee through an elevator pitch competition and a winning team is selected.

Fostering innovation and knowledge transfer

The University of Trento has been able to maintain constant communication with business companies. The aim is to establish sound cooperation networks between the academic research carried out in the laboratories and the everyday management of companies, including small ones based in Trentino and internationally-oriented ones. The University has already been proactive in fostering the attention paid by companies and the productive world to some recently-initiated areas of strategic research. Within the areas of ICT, neurosciences, integrated research, mechatronics, and civil and environmental engineering, fruitful connections have been set up, which have sometimes resulted in the mobility of PhD students and in the creation of start-ups.
These activities are primarily conducted within the Research and Technology Transfer Division at the University of Trento. The Division objectives indeed include the analysis, monitoring and evaluation of the technologies developed at the University departments, the support in creation of academic start ups and in the intellectual property. Further the Division organizes the Crash Course on research funding, intellectual property and start up creation, a seminar series open to students, researchers and enterprises.

Lino Giusti
Claudio Nidasio
Vanessa Ravagni
Research and Technology Transfer Support, University of Trento

CHAPTER
ONE

BAG ON VALVE ANALYSIS

M. Borghi, C. Bortignon, G. Bortolotti, M. Campestrin, A. Lugnan, M. Mancinelli, F. Rozio, S. Signorini, A. Trenti, G. Zendri

1.1 Introduction

COSTER Tecnologie Speciali is a leading multinational provider of aerosol spray, dispensing packaging components and filling machines. The proposed issue focused on the analysis of the fluid dynamical behavior on the Bag On Valve (BOV) spray technology. The BOV spray is based on a double compartment packaging which allows to keep separated from the propellant the content that has to be dispensed. Usually the propellant is air or nitrogen and may compromise the quality of the product. BOV technology offers many advantages with respect to traditional spray:

- the bag allows to use this spray at 4π steradian;
- separating product and propellant allows to use products which deteriorate in contact with air or other gases;
- no VOC emission using compressed air as propellant.

All this features makes BOVs a key product in the spray market. The industrial research in this sector is focusing on the vaporization of several products, from water based one to oils. BOVs present also some issues that have to be overcome. Firstly it is hard to atomize high viscosity fluids. Secondly the nebulization with BOVs is not trivial. Usually the mix of propellant and product facilitates the vaporization so the BOV technology made it more complex.
The key component for the vaporization in the BOVs spray is the so called micromist. This component is a special actuator in which the fluid passes through at the end of its path, before facing the external environment and the atomization. This micromist generate the mechanical break out of the fluid, forming the spray. The problem proposed by COSTER Tecnologie Speciali was to analyze the behavior of the micromist with viscous fluids.

1.1.1 Our strategy

The lack of a systematic comparison of the different micromist product by COSTER Tecnologie Speciali posed some limits to our analysis. We activated three different strategy:

- computational fluid dynamics (CFD) simulations on the behavior of different fluids (i.e. water and olive oil) inside the micromist;
- modeling of the behavior of the fluid in the aerosol phase with a semi analitic model;
- comparisons and analysis of the micromists produced by COSTER.

1.2 CFD Simulations

1.2.1 Starting data

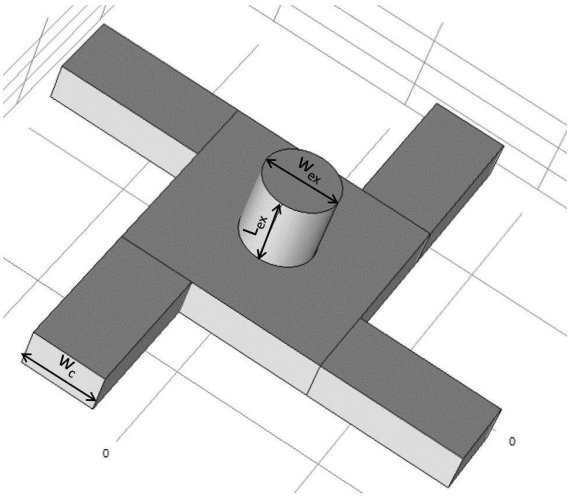

Figure 1.1: Inner part of the micromist mA: w_c channel width, L_{ex} length of the output channel and w_{ex} diameter of the output channel.

In the following, we want to find the most important BOV *geometrical parameters* that can affect the spray patter and the atomization process. We focus our simulation on a single micromist, in the following called mA, whose internal geometry is shown in Figure 1.1.
The comparison between water and oil will be carried out using the same geometry and boundary conditions, with a Finite Element Method (FEM) software. Within this frame, a detailed study on the role of the *viscosity* will be presented.

In order to evaluate the proper regimen of simulation it is necessary to know the Reynolds number of the system - Re [1]. This number is defined as:

$$Re = \frac{|u|\, d}{D_v}$$

Fluids	Kinematic viscosity (m^2/s)	Density (Kg/m^3)
water	1×10^{-6}	1000
oil	1×10^{-4}	850

Table 1.1: Fluid parameters for oil and water

where u is the average velocity, d is the hydraulic diameter and D_v is the kinematic viscosity. The fluid is laminar for a $Re < 2000$ and turbulent for a $Re > 4000$. Since D_v for a rectangular shape pipe is tabulated and d is known, it is necessary to estimate the average velocity.

1.2.2 Optical measurement of the particle velocity

The particle velocity right outside the spray nozzle can be measured by means of an optical technique. We have developed for this purpose an optical set-up.

Optical setup

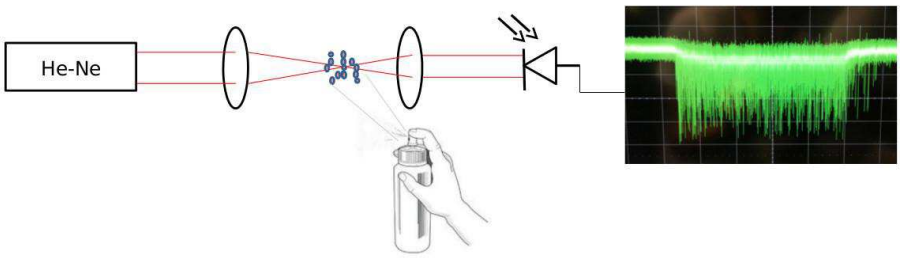

Figure 1.2: Sketch of the optical set-up.

The optical set-up used is sketched in Figure 1.2. The light source is an He-Ne laser at 633 nm. The waist of the laser beam is collimated and enlarged with the help of a beam shaper to an effective radius $r_{eff} = 3cm$. Then, using a converging lens with focal length of 23 cm, the laser beam is focused. In the focal plane of the lens, where the beam waist is minimum, the laser's light is about $1\mu m$ large. The beam is collimated again with the help of another converging lens, with focal length of 8 cm. The radiation is finally collected using an InGaAs detector with a response time of 1 ns. At a distance of 20 cm, we placed the BOV spray bottle aligned with the focal plane of the converging lens, where there is the minimum waist of the laser beam. The principle of operation is the following: when the dispenser is actuated, the particles that pass through the waist of the laser beam provide shade for a time inversely proportional to their speed. The focusing of the beam is crucial, because in this way you are sensitive at the single particle level. If you used a large spot, you would be sensitive to an average signal coming

from an ensemble of particles that cross the beam at close times. Thus in this scenario, you would not be able to have information about the single particle behaviors because you would see an overall shadow. By the means of a photo-detector and an oscilloscope one is able to track in real time the passage of the particles through the beam waist. An example of the output of the oscilloscope is shown in Figure 1.2. In particular in the picture it is reported the voltage as a function of the time. As it is possible to appreciate, the passage of the particles is seen as a series of short drops of the voltage from the mean value signal.

Results

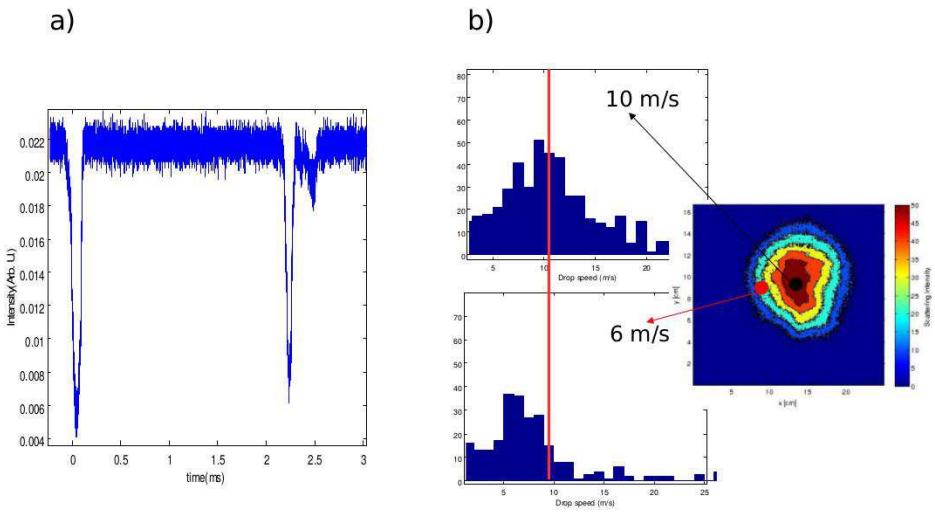

Figure 1.3: (a) Zoom of the drop of the voltage electric signal caused by the passage of two particles through the laser beam waist. (b) Two histograms showing the distribution of the particle velocity in two different regions of the spray pattern for the micromist mA.

The experimental results obtained are shown in Figure 1.3. Assuming a mean particle size $\langle \Delta s \rangle = 100 \mu m$, measured in the COSTER laboratory with a refractometry technique (discussed in section 1.4.1), one has access to the distribution of the particle velocity, i.e. for micromist mA see Figure 1.3(b). One histogram is peaked at a velocity of $10 m/s$ while the other at $6 m/s$. The two histograms indeed report the distribution of the particle velocity in different regions of the spray pattern of the micromist mA, for a fixed distance of 20 cm. In particular the upper chart refers to the case of an *in axis* measure, while the lower chart refers to the case of a 3 cm *off axis* measure.

1.2.3 Simulations

Assuming an average speed of the droplets of 10 m/s, the Re of water is about 5000 and 50 for the Oil. This value suggests that the water is close to the transition between laminar and turbulent. Considering this Re we chose to simulate the fluid as laminar for the following reasons:

1. most of the micromist have smaller channels (0.25 mm) thus a smaller Re;
2. to make a water-oil comparison using the same model;
3. this Re value is not $>>$ 4000;
4. a turbulent CFD model is far more complicated than a laminar one and requires a lot of computational resources.

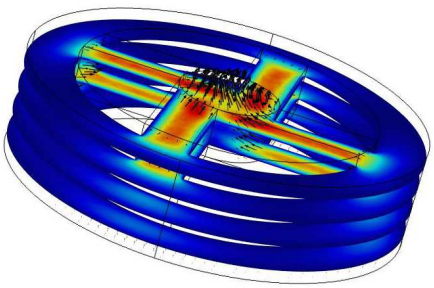

Figure 1.4: Velocity field and magnitude in a micromist. Blue, low velocity, red high.

To reduce the computational time and increase the covered parameters we decided to simulate just part of the micromist, the one in which it occurs the maximum velocity gradient. From Figure 1.4 it is understandable that the most critical part of the geometry are the 4 channels. Therefore, all the micromist were simulated starting from the channels and imposing an input fluid velocity in order to match the measured final one.

1.2.4 Results and discussion

In Figure 1.5 is shown a comparison of the fluid velocity field distribution for the water and the oil under the same simulation conditions. It is clear that the oil viscosity inhibits the vortex like fluid motion found in the water simulation. The vortex motion of the fluid is the key for the water atomization and thus the success of the micromist geometry. The high viscosity of the oil imposes a fundamental limitation on the vorticity.
Once realized that the vorticity is a crucial parameter, we tracked its behavior as a function of the liquid dynamic viscosity. We moved from a very dense oil ($D_v = 0.1Pas$) to the water ($D_v = 0.005Pas$). The results, for the exit cone

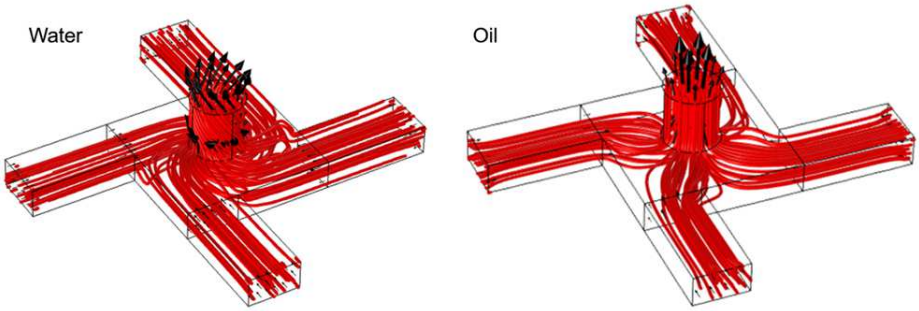

Figure 1.5: Fluid flux lines for the water and the oil in the Micromist mA.

angle[1] and the vorticity[2], are reported in Figure 1.6. The vorticity drastically decreases with the viscosity as well as the exit cone. Moreover, it seems that these two quantities are linked since they follow the same trend. The second

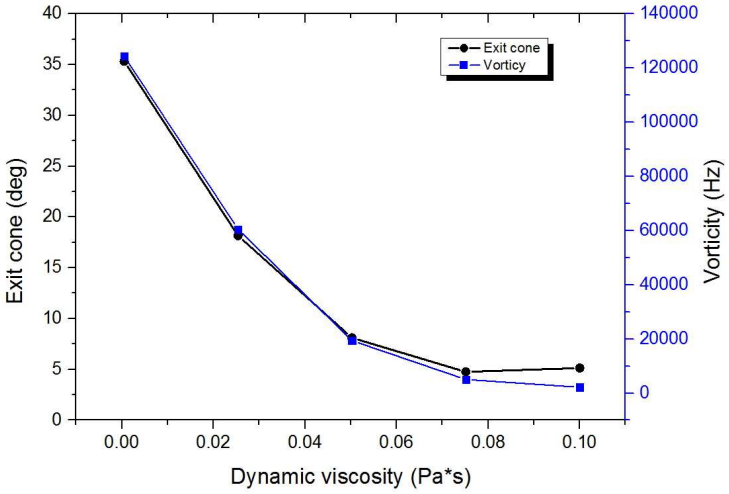

Figure 1.6: Exit cone angle and vorticity as function of the dynamic viscosity.

study investigated the link between the device geometry, i.e. exit channel length and diameter, and the exit angle for the water. The results are reported in Figure 1.7. A longer exit channel gives closer angle while a wider exit channel gives a larger exit angle. The results are in good agreement with the data observed by COSTER's engineers .

[1]The exit cone is the angle between the flux line of the dispensed product and the normal to the surface of the output orifice and it is related to the spread of the spray pattern.

[2]The vorticity is a quantity that indicates how many times per second the fluid makes a complete circle measured in Hz.

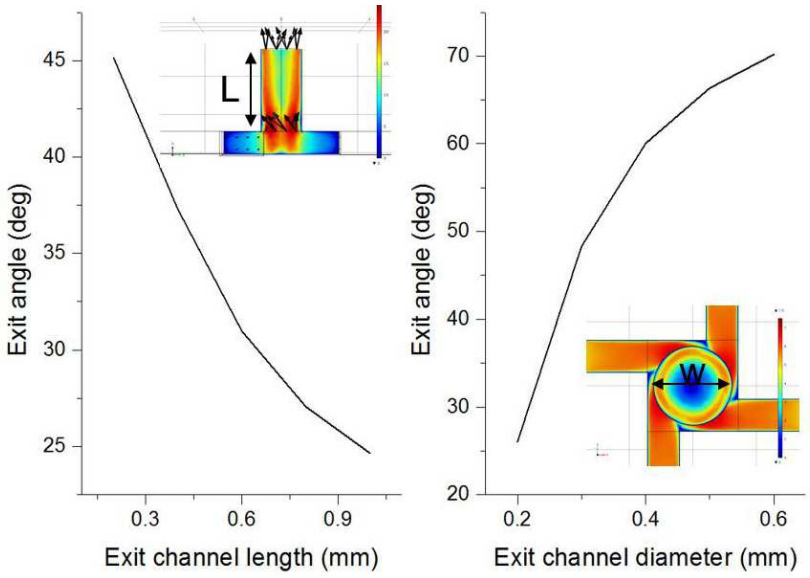

Figure 1.7: Exit angle as a function of the channel length and diameter. The insets show a vertical and horizontal cross section of the Micromist together with the velocity field.

1.3 Semi-analitical model

The second strategy was the development of a semi-analytical model. Aiming at the description of the behaviour of the product after its ejection through the micromist, we wanted to simulate numerically its propagation in air. The final task was to provide a useful tool that, combined with the CFD simulations, would predict the occurring of the nebulization for a given substance.

1.3.1 Physical model of spray atomization

We used the following assumptions:

- droplet are perfect spheres;
- droplet have all the same dimension;
- the sol-gel, from its ejection to its atomization, can be entirely described as a collection of particles

With these assumptions we reduced the problem to the analysis of particle interactions and motion laws. The interactions of a droplet are of two kinds: droplet-air and droplet-droplet. For the latter interaction the analysis of videos at high FPS of atomized water, discussed in Section1.3.1, suggested us to model the interaction between droplets as a damped[1] spring-like force. The system is then modeled by

[1]The damping is due to friction between the droplet's fluid and is modeled as a force proportional to its velocity.

the following motion equation:

$$m\ddot{r} + F_{spring} + F_{damp} + F_{air} = 0 \tag{1.1}$$

where

$F_{spring} = -kr$:
is the spring force, describing the attraction between two droplets in contact. We estimate k comparing the surface energy that has to be overcomed in order to overlap two particles [6] with the work W performed by the spring like force in bringing closer the two interacting droplets. The latter can be written as

$$\gamma \Delta A = W = \int_{2R}^{0} -kr_{DD} dr_{DD}$$

where r_{DD} is the relative distance between the two particles, γ is the surface tension and ΔA is the variation of the total surface for the process in which two distinct particles join together creating one bigger droplet with radius R[1].

$F_{damp} = -\frac{1}{2} C_d \rho_f A v_{DD}^2$:
is the viscous drag due to droplet-droplet interaction, with ρ_f density of the fluids, v_{DD} is the relative velocity between two droplet, C_d is the drag coefficient and A the effective surface for the drag. The C_d coefficient is strictly related to Re, as reported in Figure 1.8. Observing that in our conditions $10 \leq Re \leq 100$ we fitted the experimental data of C_d in this range, as shown in Figure 1.8.[1]

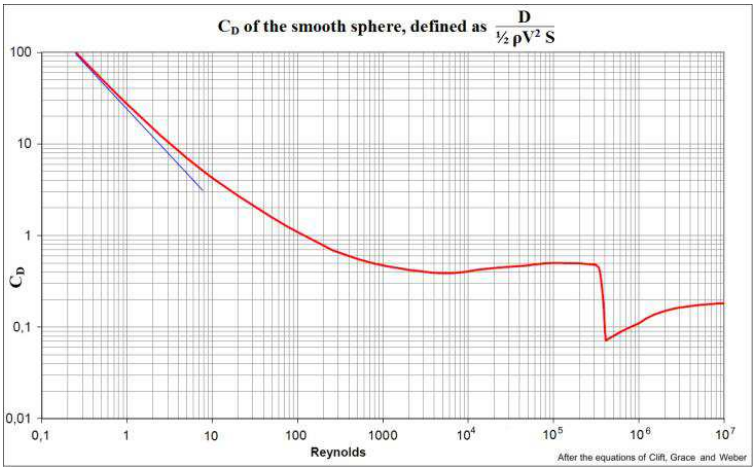

Figure 1.8: Relation between C_d and the Reynolds number for a sphere [7].

[1] We also investigated experimentally this value, discussed in the following paragraph. Its results were in agreement with this fit and allowed us to model the drag.

Coefficient	Value	Source
R Droplet radius	10-100 μm	Measured
ρ_a air density	1.2922 kg m^3 @ 300 K	[3]
ρ_f fluid density	1000 Kg m^3 (water), 850 Kg m^3 (olive oil)	[4]
γ surface tension	0.0728 $\frac{N}{m}$ (water), 0.0320 $\frac{N}{m}$ (olive oil)	[5]
μ dinamic viscosity	0.001 Pa s (water), 0.1 Pa s (olive oil)	[4]

Table 1.2: Main parameters used for the semi-analitycal model.

$F_{air} = -\frac{1}{2}\rho_a v^2 C_d A$:
is the drag due to friction with air, with ρ_a density of the air, v the velocity of the droplet respect the air. We model the drag with the Rayleigh equation considering that Re is always greater than 1[2].

Experimental study of the droplet-droplet interaction

In order to have an experimental insight into the interaction between two droplets, we set up an experimental apparatus, shown in Figure 1.9.

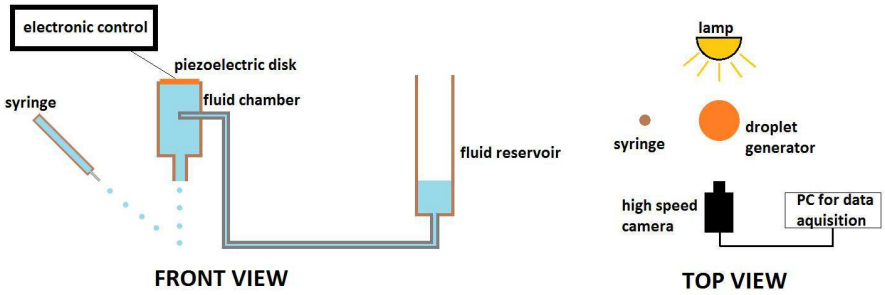

Figure 1.9: Scheme of the experimental apparatus used for the study of the droplet-droplet interaction.

A droplet generator produces a stream of identical droplets at a controllable frequency. This generator consists of a chamber sealed at the top with a piezoelectric disk. At the bottom there is an outlet from which droplets are ejected. This chamber is connected with a tube to a fluid reservoir, open at atmospheric pressure. The height of the reservoir is adjusted to obtain hydrostatic equilibrium: a stable meniscus forms at the outlet, no fluid flows out nor air is drawn into the chamber. The polarity of the piezoelectric is inverted causing a contraction of the disk. Consequently to this contraction a droplet of the fluid is expelled from the chamber. The electronic control of the piezoelectric disk is made with an Arduino board. The second jet of droplets was manually generated with an insulin syringe. The recording system consisted in a high speed camera (Redlake 1000s). In Figure 1.10 it is shown an example of the frames extracted from a high speed

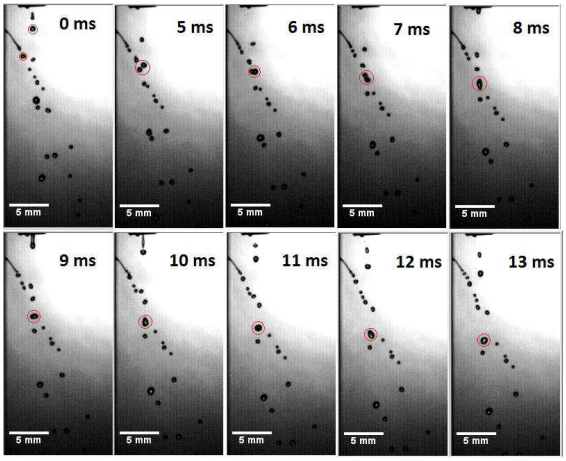

Figure 1.10: Frames recorded with the high speed camera showing the fusion of two interacting droplets.

video of the collision of two droplets. In order to evaluate the drag coefficient of the interaction between droplet we considered only the fusion of two droplets after the collision[1] As shown in Figure 1.11, right after the collision it is necessary some

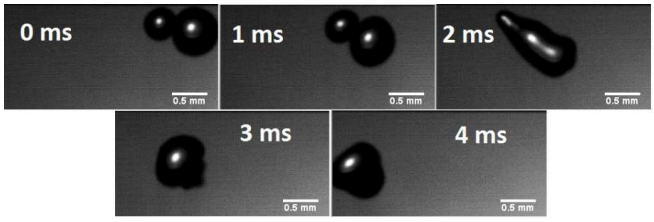

Figure 1.11: Zoom of the first phases of the fusion of two droplets.

time in which the surface of the merged droplet oscillates with an exponentially damping. This experimental observation supports the theoretical assumption of the interaction between two droplets as a damped spring-like force. We measured the area of the two interacting droplets and of the merged one. Figure 1.12 shows an example of the graphs obtained. Data after the collision were fitted with a decreasing exponential function $y(t) = Ae^{-\frac{t}{\tau}+y_0}$, where τ is the decay time. The obtained values for τ were in the range from 3 to 10 ms, in agreement with the linear fit of the C_d in the Re range 10-100.

[1]It is noticeable that, besides the fusion of two droplets, other situations could be observed. For example when one of the two colliding droplets is much bigger than the other, no fusion is observed but only a collision that deviate its trajectories.

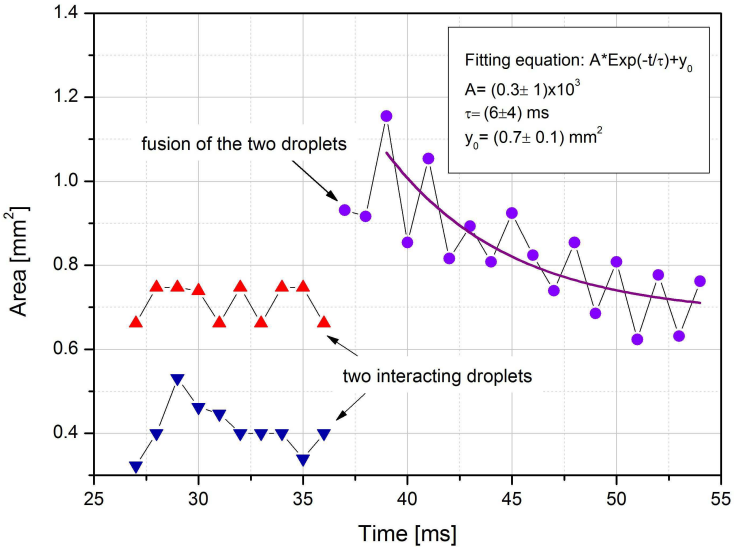

Figure 1.12: Measured area of two interacting droplets before and after fusion as a function of time.

1.3.2 Results

The simulation procedure consisted in the solution of 1.1 using as initial condition the velocity field obtained by the CFD simulation[1]. Due to the limited computational time available, we considered only 100 particles. The Ordinary Differential Equation (ODE) solver returns the trajectory of each particle. Through this paths it is possible to understand if the atomization occurred. In Figure 1.13 are reported the results for water at different fluid vorticity. As the velocity increases the atomization becomes more evident. With this simulation it was obtained a radius of the pattern of 15 cm at a distance of 20 cm, value close to the experimental one.

1.4 Optimization process

Our third strategy involved the elaboration of an optimization process for the design of a micromist.

1.4.1 Introduction and theory

This process of optimization consists in finding the best set of parameters which maximizes the performance of the micromist. Several structural parameters influence the shape of the output flux. Among these, we chose as most significant

[1]The simulation was performed only for the mA micromist, but it could be easily extended to any micromist.

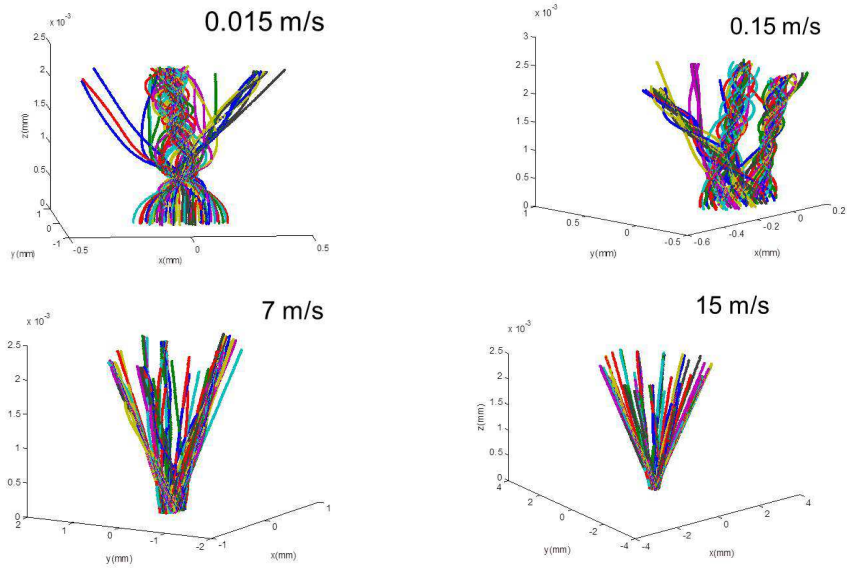

Figure 1.13: Water droplet trajectories for micromist mA with increasing vorticity. As velocity increases, the trajectories become more and more separated, indicating the occurring of atomization.

ones the channel width w, the chamber diameter d, the orifice diameter φ and the orifice thickness Δ . The performance is evaluated on the aperture cone, the discharge rate, the output velocity and the fluid vorticity (Figure 1.14). So the input parameter is a vector $\vec{x}$ defined by the geometrical features

$$\vec{x} = (w, d, \phi, \Delta)$$

The process of optimization is based on finding a relation between the input parameters and the output ones. This relation can be very complex, even not analytical. However, focusing on small displacements of the input parameters $\vec{x}$ with respect to a reference geometry $\vec{x_0}$, we can linearize the outputs P as:

$$P(\vec{x}) = P(\vec{x_0}) + \vec{M} \bullet (\vec{x} - \vec{x_0}) \tag{1.2}$$

where $\vec{M}$ is a set of 4 coefficients, each describing the behavior of P with respect to one of the four input feature. To find M_j it is necessary to evaluate P in a geometry which differs from the reference one only by a small displacement in the feature x_j. In such a way that

$$M_j = \frac{P(\vec{x}) - P(\vec{x_0})}{x_j - x_{j_0}}$$

This task can be accomplished experimentally by realizing 5 different micromist, one used as reference and the other 4 having displacements along x_j in such a

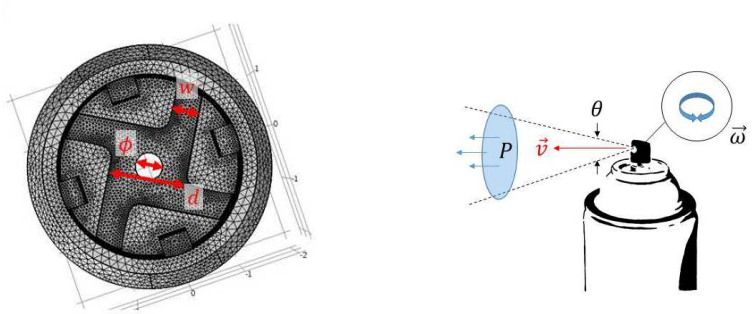

Figure 1.14: Micromist's geometry: w channel width, φ orifice diameter, d chamber diameter. Sketch of the output parameters, or spray performance. P is the discharge rate, θ the aperture cone, $\vec{v}$ the velocity and $\vec{\omega}$ the vorticity.

way that for the j^{th} micromist we have $x^{(j)} - x_0 = x_j^{(j)} - x_{j_0}$. For these analysis we tried 3 different approaches:

1. self prototyping of micromists using a 3D printer;
2. perform measurements at COSTER of a set of micromists which is as close as possible to the reference one;
3. use the data collected from a FEM simulation.

Self prototyping of micromist with 3D printer

In collaboration with the MUSE FabLab we attempted to print with a 3D printer the micromist mA[1], see Figure 1.15. The printer's resolution was not able to elaborate all the features of the micromist.

Figure 1.15: Picture of the micromist prototype developed to FabLab at MUSE.

[1]The 3D printer used at MUSE FabLab has a layer resolution of 0.02 mm, a nozzle diameter of 0.4 mm and a printing speed of 40 mm/s.

Measurement at COSTER research and development laboratory

Aiming at a useful set of micromist we performed some measurements at COSTER using selected micromists mounted on a BOV spray containing water. For each micromist we measure four different quantities:

- **dischage rate**: comparing pressure and weight of the spray before and after a fixed nebulization;
- **spray pattern**: using a pinhole that rotates at a fixed angular speed, see Figure 1.16
- **particle size**: with a laser diffractometry technique.

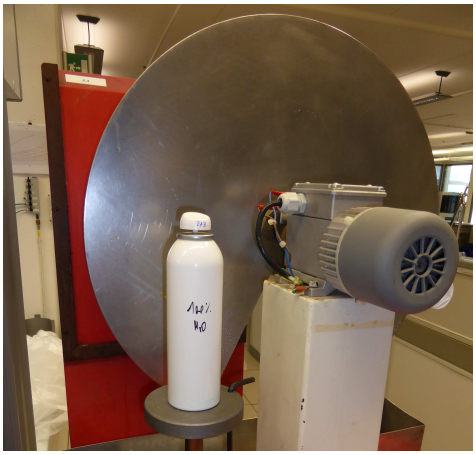

Figure 1.16: Picture of the pinhole used for the spray pattern measure.

The analysis of the data has highlighted the absence of a proper set of micromist for this study.

Finite element method simulations

With a FEM simulation approach we fixed the reference parameters $\vec{x_o}$ and performed a parametric sweep along the different directions x_j. The data obtained allowed us to evaluate the aperture cone, the discharge rate, the output velocity and the fluid vorticity. In Figure 1.17 is shown an example of the simulated curves for the discharge rate. The slopes of these curves are related to the M_j coefficients. We point out that the FEM linear model is just an approximation of the aerosol behavior. An experimental evaluation of the performance is strongly suggested.

1.4.2 Results and discussion

Table 1.3 compares the predicted values obtained using equation 1.2 with the ones obtained by a direct solution of the FEM equations. The agreement between

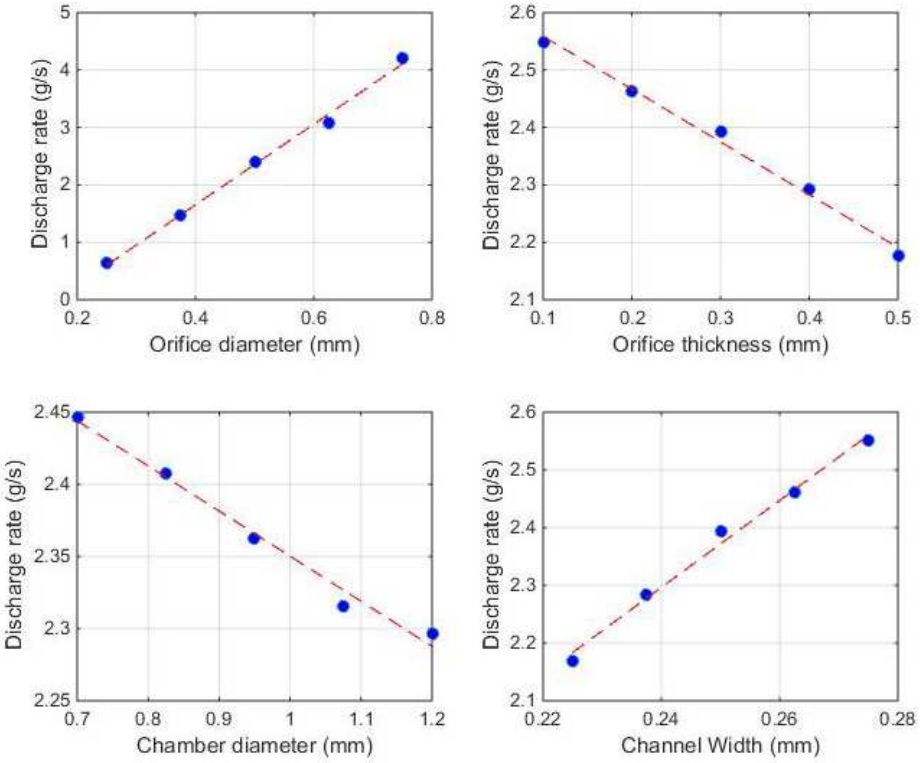

Figure 1.17: The discharge rate of the micromist as a function of the orifice diameter, the orifice thickness, the chamber diameter and the channel width. Blue dots are from FEM simulations, red dashed lines from linear fit of the data.

Output parameter	Linear model	FEM results
Discharge rate (g/s)	1.21 ± 0.1	1.42
Cone aperture at 15 cm (cm)	6.3 ± 0.7	6.8
Fluid velocity (m/s)	0.71 ± 0.04	0.71
Vorticosity (1/s)	$(5.0 \pm 0.8) \cdot 10^3$	$5.4 \cdot 10^3$

Table 1.3: Comparison between the output parameters predicted by the linearized model and FEM simulations.

the two results confirms the validity of the linear approximation approach in this range. The usefulness of this method relies on the possibility to use a reverse engineering approach to find the set of parameters which produces the desired output performance.

1.5 Laser Sheet Imaging

1.5.1 Experimental evidence

The spray patterns obtained at COSTER's laboratory, described in section 1.4.1, introduced some problems in our measurement:

- the paper in which we had to spray reacts chemically to alcohol but we needed to use pure water;
- it was not possible to measure the spray intensity;
- with large cone aperture we had to change the experimental conditions;
- the fluid may bounce on the machinery and spoil the pattern;
- the output is a stain on paper and nota digital data[1].

In order to obtain a good spray pattern for pure water we developed an apparatus for the spray pattern digital imaging. In our set up the spray passes through a laser sheet, in such a way that its liquid droplets diffuse the impinging light and can be photographed. We used a helium-neon laser with a cylindrical lens to obtain a laser sheet. We acquired the picture with a digital camera Nikon D80 with a 18-200 mm optics.

1.5.2 Results

In Figure 1.18 are shown a spray pattern acquired at COSTER lab[2] (a), the one taken with our laser sheet imaging (b) and its the elaboration with Matlab (c).

1.6 Conclusions and possible outcomes

During the IPSP week we developed four different strategy of solutions.

- We simulated the behavior of the fluid inside the camera, highlighting the keystone of this problem: the fluid vorticity. This parameter seems to be the one on whichthe atomization depend the most.

[1] We had to take a picture of the paper with a reference object, import the picture in Matlab and then elaborate the data.

[2] Despite this spray pattern is not suitable for commercial purpose, we chose to present this pattern due to its typical shape, demonstrating the agreement of the data acquired with the two techniques.

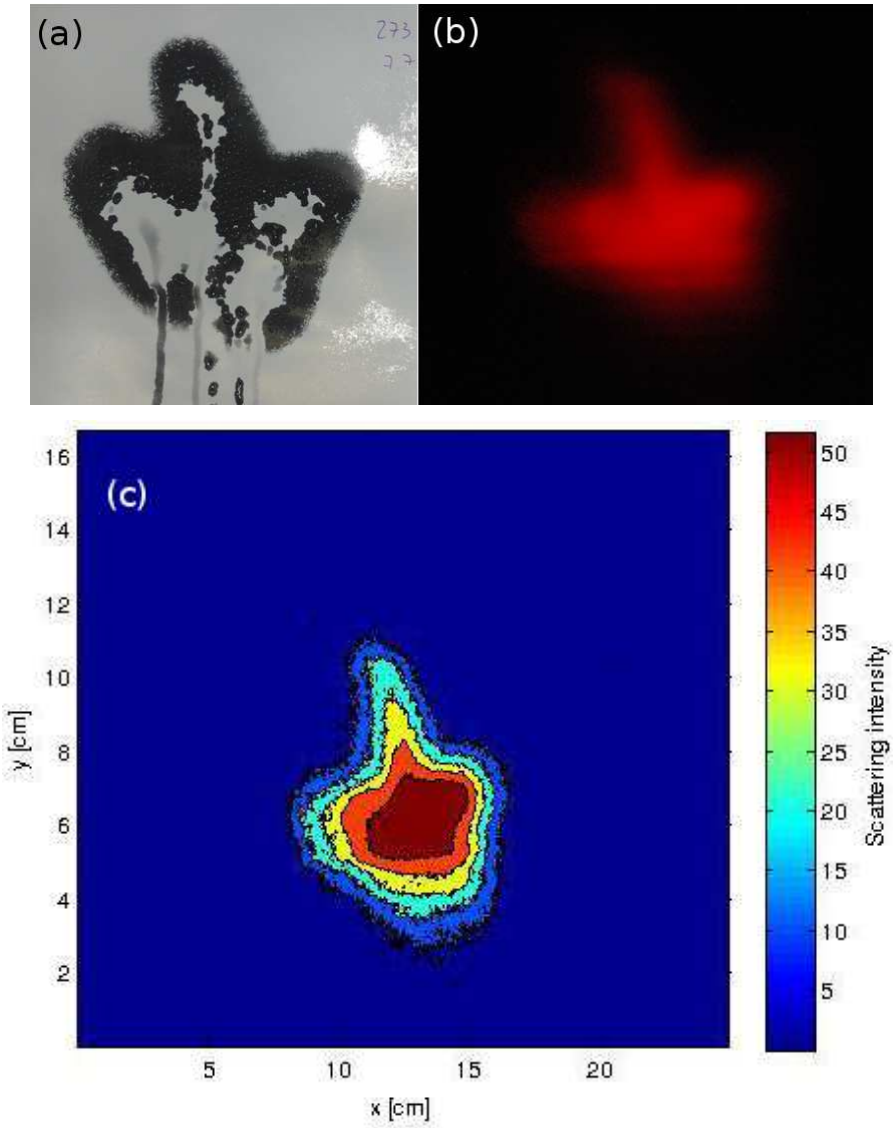

Figure 1.18: Example of spray pattern obtained with COSTER's apparatus (a) and the same spray pattern obtained with our laser sheet imaging (b). In (c) is shown an elaboration with Matlab obtained with the aid of a space reference. This picture allows to recognize both the spray pattern and its intensity as a function of space.

- It has been developed a brand new model able to predict the behavior of the product right after the micromist orifice. The results of this model are in good agreement with the experimental data and predict whether a fluid atomizes or not.
- We designed and implemented an optimization process able to predict the micromist technical features necessary to get and fulfill the output characteristics of the final outcome.
- It was developed a laser sheet imaging technique able to analyze the shape of the spray cross section and its intensity.

We would also point out three different roads that should be investigated for a deeper comprehension of the problem:

- We suggest to prototype a whole variety of micromist that are varying one single feature. This could provide the experimental data necessary to improve the optimization process and base it on real micromist product by COSTER.
- We propose to deeply investigate whether a threshold fluid vorticity exists or not. Our simulations, that have to be improved, suggest that it should exist a threshold vorticity above which the atomization occurs.
- We point out a laser sheet imaging apparatus as a solution to measure the spray pattern for any fluid. Our rudimental apparatus could be properly improved in order to measure both the spray pattern and the fluid density distribution.

BIBLIOGRAPHY

[1] https://en.wikipedia.org/wiki/Reynolds_number

[2] T.E. Faber. *Fluid dynamics for physicists*. Cambridge University press,1995

[3] https://en.wikipedia.org/wiki/Density

[4] http://www.engineeringtoolbox.com/

[5] http://physics.about.com/

[6] https://en.wikipedia.org/wiki/Surface_energy

[7] https://en.wikipedia.org/wiki/Drag_coefficient

CHAPTER
TWO

SKI-BOOT STRESS MAP

S. Amirabdollahian, M. Azzolini, M. Bertolla, C. Castellan, L. Cossu, E. Demenev, D. Giovannelli, C. Piotto, D. Roilo, M. Secchi, S. Tondini

2.1 Introduction

2.1.1 The company

LA SPORTIVA was born in 1928 when Narciso Delladio hand-crafted wooden leather boots for many lumberjacks and farmers of the Fassa and Fiemme valleys (Dolomites, Italy). After the war, the demand for boots increased obliging the hiring of new workers: the good name of "Calzoleria Sportiva" crossed the boarders of the valleys. Starting from here LA SPORTIVA's history continued to grow. Now the firm produces in Fiemme Valley boots and shoes for all kind of outdoor activities, from trekking/mountain running to climbing, categories in which LA SPORTIVA S.p.A. has the market leadership. Recently the company entered the ski-mountaineering segment and the apparel market with a complete selection of technical clothes for running, climbing and ski-mountaineering. LA SPORTIVA produces mainly in his headquarter at Ziano di Fiemme, but is distributed in more than 70 countries worldwide. LA SPORTIVA's main aim and the basis of its activities is customer satisfaction while respecting the surrounding environment. To achieve this aim, the firm commits itself daily, transforming the requests into requisites throughout the production system, to create the most efficient and advanced products. The R&D department is constantly searching for innovative and purposeful solutions, to guarantee a product able to meet the most demanding and advanced technical requirements, as well as offering safety and comfort in terms of use, thanks also to state-of-the-art equipment.

2.1.2 The problem

Ski-mountaineering, where athletes follow challenging trails on winter alpine or american terrain, and freeride on unmarked or unpatrolled areas, either inside

Figure 2.1: Rendering of the ski-boot model Spectre produced by LA SPORTIVA.

or outside of a ski resort's boundaries, are spreading more and more. Such a market is demanding fat skis, performing bindings, and high flex boots, able to match unprecedented rigidity while keeping down the weight. Within this frame LA SPORTIVA is presenting the ski-boot named Spectre (Figure 2.1), which results from combining four-buckle downhill performance with two-buckle touring comfort and ease on the up. The shell is made of lightweight Grilamid while the Carbon reinforced Vertebra drives the powerful 120-Flex downhill performance. The 60° range of motion and EZ Flex tongue allow for a comfortable walking and make the boot well suited for technical climbing. This product plays a key role in terms of marketing, and an improved design could surely lead to an overall sales increase. Therefore, LA SPORTIVA asked for an experimental/simulative study on the structural behavior of the boot, where special attention has to be paid to the points of maximum deformation during use. The evaluation of constraints and loads experienced by the boot under test represents the first step of a physical analysis [1]. The recorded data could be useful to calibrate a numerical simulation, in order to obtain the same deformations as in the laboratory. This, in turn, constitutes a tool, which could be applied to any other ski-boot, allowing for the realization of novel competitive geometries in terms of flex and weight.

2.1.3 Equipment

LA SPORTIVA shared:

- 1 pair of ski-boot model Spectre
- 1 set of components of a ski-boot (left feet) model Spectre
- 2D/3D Cads and Finite Element Method (FEM) simulations of the ski-boot model Spectre
- Free access to the benchmarks and test facilities of the LA SPORTIVA's headquarter at Ziano di Fiemme.

University of Trento made available:

- Strain gauges, load cells and glues (evaluation samples provided by HBM Italia S.r.l.)
- Strain gauge bridge amplifier HBM QuantumX MX1601B
- Thermocamera model FLIR 250 IR

2.1.4 Approaches to the problem

The team decided to follow three different approaches to the development of a tool to map the stress of a ski-boot under test on a benchmark. In particular, the **strain gauge sensorization**, the **infrared thermography** and the **photoelastic measurement** of surface strain were attempted. The activities have been split among the team members. However, some tasks required the effort of the entire group to be accomplished.

2.2 Strain gauge sensorization

2.2.1 Measuring the strain through a strain gauge

Local deformation measurements on the surface of a ski-boot were implemented using strain gauge sensors placed in the most important points of the specimen. In general, a strain gauge consists of an insulating flexible base which supports a metallic foil pattern (see Figure 2.2(a)); the grid pattern maximizes the amount of metallic wire or foil subject to strain in the parallel direction whereas the cross sectional area of the grid is minimized to reduce the effect of shear strain (angular distortion) and Poisson strain (elongated body changes its cross section). When the metallic pattern of the gauge is deformed, it results in a change of its

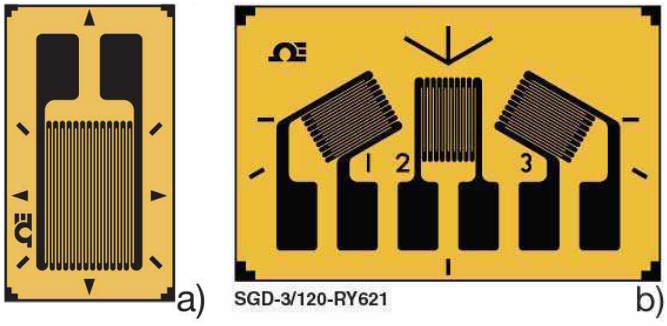

Figure 2.2: Schematics of the used strain gauges: (a) linear strain gauge, (b) three foil pattern strain gauge.

	HBM model	Grid numb.	Nom. res. [Ω]	$\mathcal{F}$
A	6/120 RY81	3	120	$2.05 \pm 1\%$
B	6/120 LY41	1	120	$2.05 \pm 1\%$
C	6/350 LY41	1	350	$2.10 \pm 0.5\%$

Table 2.1: Strain gauges applied to the ski-boot. The gauge factor $\mathcal{F}$ is referred to the temperature of 24°C.

electric conductivity, and therefore measuring the resistance in a stressed state it is possible to estimate the absolute deformation using the linear equation:

$$\frac{\Delta R}{R_0} = \mathcal{F}\varepsilon \tag{2.1}$$

where ε is the measured strain, $\mathcal{F}$ is the gauge factor characteristic of the sensor, ΔR is the resistance variation, and R_0 is the resistance of unstrained gauge [2].
During the experiments three different models of strain gauges were used. The first two models (Figure 2.2(a)) are linear strain gauges optimized for different materials and with different nominal resistance of 120 Ω (code B, optimized for steel) and 350 Ω (code C, optimized for PMMA). The third type of the sensors (Figure 2.2(b)) consists of three foil patterns on a single substrate aligned $-45°$, $0°$, and $+45°$ relatively to the main axis of the gauge (code A) with a nominal resistance 120Ω: the measuring elements are located very close to each other allowing estimation of a total strain in the given point (not only 1-D along the gauge axis). It is very important to note that the strain gradient on a ski-boot might be very high and its value may be very different on the scale of few millimeters and thus estimation of absolute strain using 3-axis gauge should be made with particular attention. Table 2.1 summarizes the used sensors with their main characteristics. The measurements of the strain gauge resistance were performed using QuantumX MX1601B data acquisition system. In order to provide the best performance, all the sensors were connected via Wheatstone bridges [3]. The primary benefit of a Wheatstone bridge is its ability to provide extremely accurate measurements of small variations of resistance value.
In order to keep the lowest measuring resistance, and thus obtaining the most precise measurements, points A and B of the bridge (Figure 2.3) should be placed as close to the sensor as possible. For this purpose an additional socket was installed on the specimen: all the gauges were connected to the socket using copper wires of 0.3 mm diameter (length not exceeding 30 cm, parasitic resistance below 0.1 Ω), and from the socket, every gauge was connected to the DAQ through 4 wires.

In general, strain gauge measurements are very precise, however there are many factors that could spoil the experiment accuracy. Within the conducted experiments, our team tried to minimize all the possible sources of errors and keep the experimental conditions as good as possible. The aspects that were dealt with particular attention are:

- **orthogonal deformation:** although the strain gauges are designed to work in only one direction, deformation on the other directions as well as bending

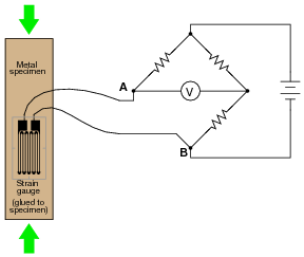

Figure 2.3: Schematic of the connection between the strain gauges and the data acquisition system.

can also influence the measurements. In order to minimize the influence of side effects, the strain gauges were placed in points with assumed minimum bending potential and aligning them to the expected axis of elongation;

- **glue layer thickness:** a thick layer of glue can potentially absorb very significant amount of strain and thus it should be kept to minimum: when installing the sensors, the glue layer did not exceed 100 μm which should be enough to avoid any impact on the final result;

- **temperature dependence:** the resistivity and strain sensitivity (namely gauge factor) of all known strain-sensitive materials vary with temperature. This variation consequently may impose significant deviation to the measured values and thus should be taken into account. For the used gauges, the strain sensitivity was documented and the temperature variation was corrected at the data processing step according to the datasheet suggestions.

2.2.2 Feasibility test

In order to verify the performance of the sensors, a preliminary experiment was designed. In this experiment, each type of sensor was installed on a uniform plastic specimen. As recommended by constructors, the strain gauges were applied to the surface after an adequate cleaning procedure, in order to obtain the maximum possible performance from the sensors applying them on a chemically cleaned surface with an adequate roughness and alkalinity (pH 7). The surface was degreased with a solvent, grinded with the sandpaper, then a neutralizer was applied. Cyanoacrylic glue was used to attach the strain gauges on the specimen: the sensor was firstly aligned in the desired position and fixed with an adhesive tape, then the glue was applied on the back side of the sensor paying attention to the amount of material added, finally gluing it to the surface.
After the gluing step, the specimen was subjected to the various forces applied along the gauge axis. Applying different weights ranging from 0 to 70N, response curve for each of 3 sensors (5 measuring channels) were recorded (Figure 2.4 (top)). Although mechanical properties of the plastic were unknown not allowing precise calibration of the sensors and verifying absolute values of the strain, the experiment resulted in three important conclusions:

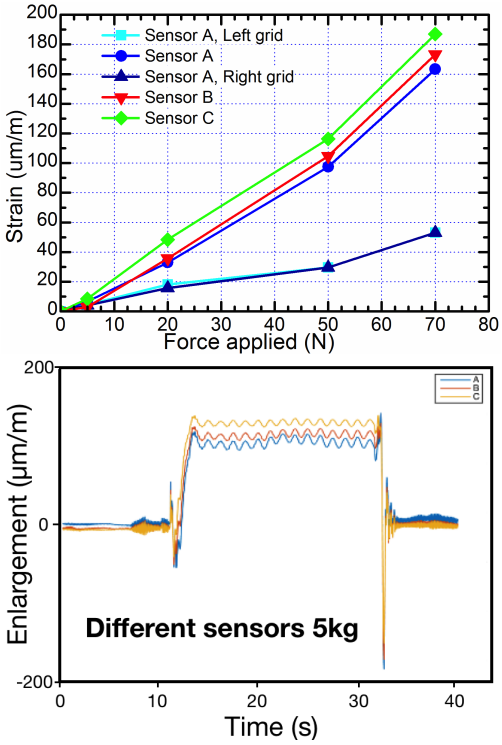

Figure 2.4: (top) Strain measured on a uniform plastic specimen for the preliminary test, (bottom) strain as a time function during application/removal of the strain.

- all the sensors showed near-linear dependence versus applied force;
- the absolute values are within 8% of difference, which is being satisfying taking into account all the possible sources of the errors (such as non-uniform material of the specimen, small axial misalignments among the sensors, etc.);
- 45° aligned sensors resulted in much lower values of strain which is assumed being result of the Poisson strain (the specimen experienced orthogonal shrinking due to elongation).

Moreover, it was confirmed that the memory effect of the sensor is negligible at the timescale of the experiment: the measured resistance returns to its baseline value as soon as the applied force is removed (Figure 2.4 (bottom)).

2.2.3 Ski-boot specimen

In total 24 strain gauge sensors were installed on the working specimen using the gluing procedure previously described. The location of the sensor is shown in Figure 2.5. In order to minimize mechanical damage of the wiring, epoxy glue was used to cover all the gauges and to attach copper wires to the boots.

Figure 2.5: Gauges location on a ski-boot specimen.

The used data acquisition system allows measuring up to 14 channels simultaneously. Since the amount of sensors exceeded the number of channels, all the sensors were divided into two groups (namely the left and the right side of the boot), and only one group of the sensors could be measures at a time. For this purpose, two separate connection sockets were installed. During the experiment on the testing stand at LA SPORTIVA headquarter, beside the strain gauges, a load cell sensor was analyzed. The cell was installed on the working piston allowing to synchronize measured strains and relate them to the load applied to the boot (Figure 2.6).

2.2.4 Testing machine

In the testing machine, the sole of the boot is fixed and an adjustable pressure is continuously applied on the back of the boot through a piston, in order to simulate the skiing action.

2.2.5 Piston calibration

The aim of the piston calibration is to correlate the pressure that can be set on the testing station with the force actually applied to the boot. This was realized by means of a load cell placed in between the boot and the piston. The acquired data are reported in Figure 2.7 (scatter points).

The theoretical force (blue line) was calculated by multiplying the surface on which the pressure is applied by the pressure value itself. The theoretical prediction lies inside the error bars of the measured values. A linear relation,

which connects the value of the pressure set during the test with the force applied to the boot can be obtained by fitting the experimental data. The relation is reported in the red line of the graph.

Figure 2.6: Load cell location in the testing chamber (red arrow).

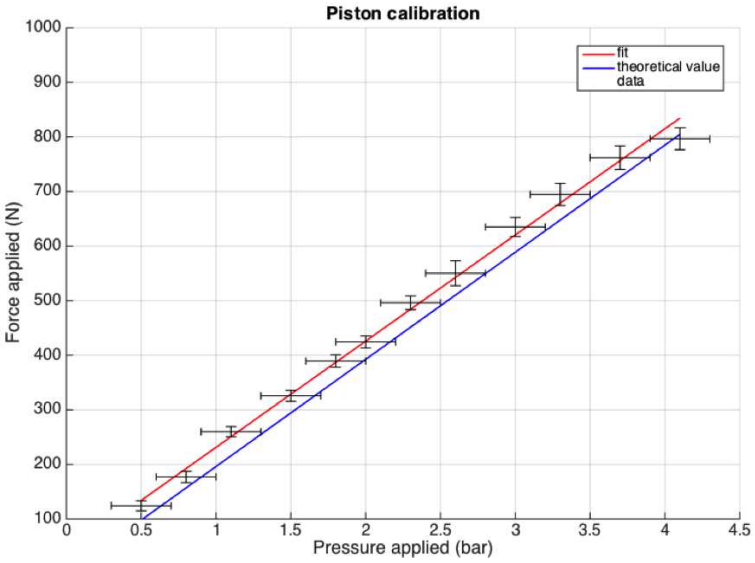

Figure 2.7: (scatter points) measured values of force as a function of the pressure set within the test chamber; (blue line) theoretical prediction of the force applied to the boot; (red line) linear fit preformed on the experimental data.

Component	Young modulus
Shell	900 MPa
Cuff	4400 MPa
Shell tendon	200000 MPa

Table 2.2: Young modulus of the different ski-boot components.

2.2.6 Strain to stress conversion

In order to obtain the stress distribution on the boot, the relative elongation (E) of each strain gauge was acquired and multiplied by the Young modulus Y of the material, which the strain gauge was applied on. In fact, the stress S is given by:

$$S = YE. \tag{2.2}$$

The stress distribution map was obtained considering the Young modulus of the different boot components listed in Table 2.2. First of all, the signal acquired from the strain gauges was corrected in order to consider the temperature effect on the sensors response. Then, the elongation was multiplied by the Young modulus, to obtain the stress applied on the searched region.
During the tests, the piston was kept in motion, producing a periodic force applied to the boot. Therefore, the signal transduced by the strain gauges resulted, in turn, periodic. Hence, the maximum elongation, which corresponds to the maximum intensity of the acquired signal, was calculated as the mean value of many local maxima of the acquired signal. The error bars were obtained considering the standard deviation of the local maxima.

2.2.7 Stress measurements

The stress distribution map was realized by varying the pressure values, i.e the force applied to the boot.
Figures 2.8 and 2.9 show the stress distribution on the different parts of the boot. In particular, in Figure 2.9, the arrows indicate the strain gauges elongation direction.

Initially we analysed the external area of the boot (Figure 2.8 (left column)), concluding that the region that is more stressed is the cuff. Secondly, we analysed the internal part of the boot (Figure 2.8 (right column)), confirming that the cuff is more stressed than the shell. Moreover, the analysis of the sole (Figure 2.9 (top)) shows that also this area is less stressed than the cuff. Finally, we found that the most stressed area is the steel tendon (Figure 2.9 (bottom)). The scattered behaviour could be attributed to the fact that this area is highly movable during the skiing activity simulation and the presence of a connection pin makes the connected parts vibrating dramatically.

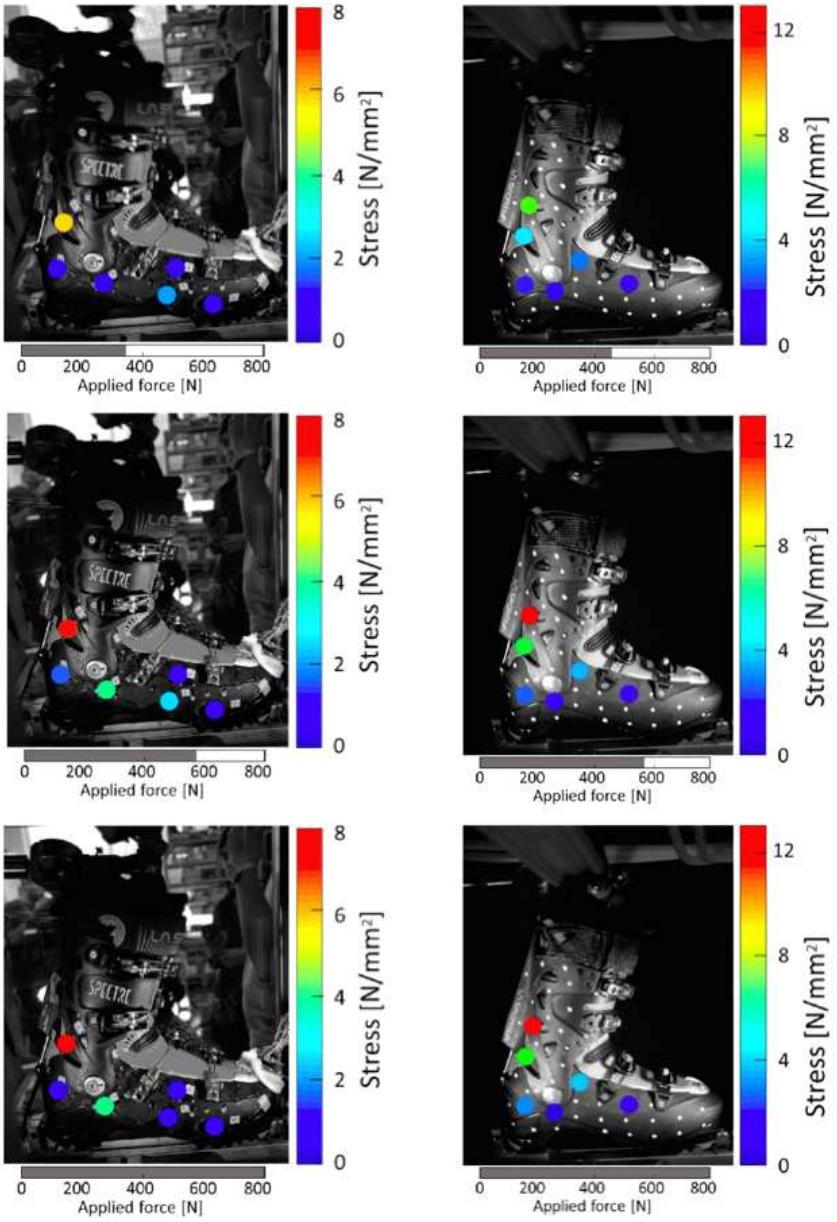

Figure 2.8: Stress values as a function of the applied force as they have been measured from the strain gauges placed on the external side of the boot (left column) and on the internal side of the boot (right column).

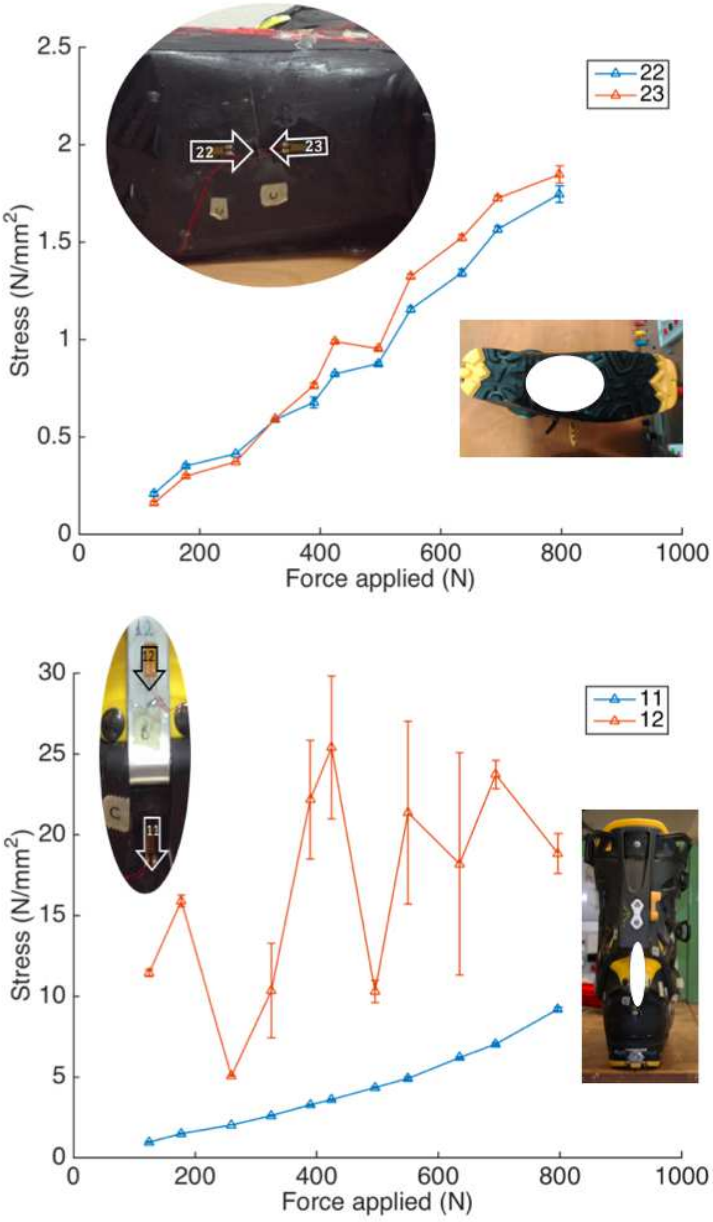

Figure 2.9: Stress values as a function of the applied force as they have been measured from the strain gauges placed in the sole of the boot (top chart) and in the tendon of the boot (bottom chart).

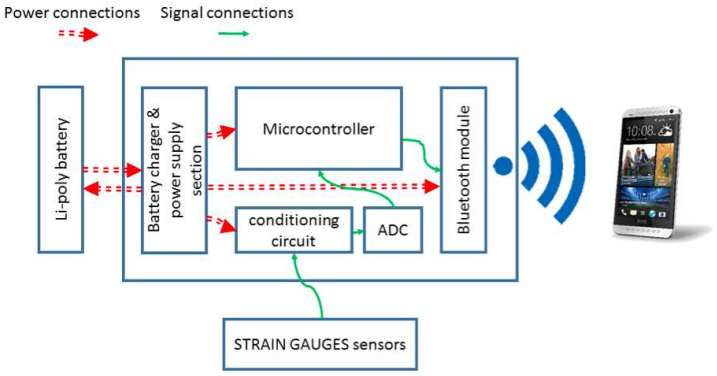

Figure 2.10: Block diagram of the proposed mobile embedded version of the system.

2.2.8 Future perspectives

The experimental setup is well suited for in-door laboratory tests. Even if the testing machine is cooled down in temperature it is still far from reproducing the real usage condition of a ski-boot. In fact, the tests were performed with piston force ranging from 120 N to 800 N, but the real range of forces applied on the boot during normal skiing remains unknown. A significant improvement can be obtained via a dedicated system for real-life usage monitoring. The strain gauges installed on the specimen can be easily used in out-door condition (e.g. on a ski slope), in order to evaluate the strain that the ski-boot experiences. For doing this, a first raw project has been developed, consisting in a mobile embedded version of the system, enabling to perform the same measurements.
All the data acquisition system should be realized as a stand-alone device which would not influence the measurement. Figure 2.10 shows a block diagram of the proposed stand-alone solution. The system is characterized by a typical embedded system topology based on microcontroller. Its main blocks are: a microcontroller, a power supply section, a conditioning circuit, sensors, an ADC and a Bluetooth module. In the following each module task is going to be explained with some relevant points regarding the design.

- **Microcontroller:** it is the core of the system and manages data acquisition, Bluetooth module functionalities and all other configurable components of the circuit (battery charger behavior, conditioning circuit gain, etc.). Since raw data will be sent through Bluetooth, no particular signal processing feature is needed; during the cost estimation an STM32 microcontroller was proposed, but every similar low power/high performance microcontroller can be used.

- **Power supply section:** it feeds the whole board with the correct stabilized voltage and manages the battery charge: the BQ24075 is suggested as core component for power supply section.

- **Conditioning circuit:** it is mandatory to convert the resistance variation

of the strain gauges into voltage variation that can be acquired by an ADC. This is usually performed via a Wheatstone bridge followed by an amplifier, since voltage variation at amplifier input is very small compared to its absolute value, a high common mode rejection ratio is needed. These requirements are fulfilled by Instrumentation Amplifiers, which are widely used to amplify the small output of the strain gauges.

- **Sensors:** the strain gauges used during the IPSP week can work on plastic surfaces in cold environment, therefore ther is no need of selecting different sensors. However, adding a temperature sensor can be useful to measure the actual ambient temperature during the test in order to take into account the temperature dependence of the gauge factor. Since strain gauges are analog sensors, to simplify the design, an analog sensor even for temperature acquisition was proposed. Moreover, since temperature can significantly vary on different boot use location, it is better to include more than one temperature sensor.

- **ADC:** since the signal from strain gauges can be characterized by wide dynamic range, especially when subjected to impulsive impacts exerted on boots during skiing, a conservative design choice is to sample signals at 24 bit. Most of microcontrollers include an ADC that could be used, but it is very uncommon to find a 24 bit ADC embedded in a microcontroller (usually they have 12 or 16-bit ADC), then an external ADC was included in the design. LTC2418 was selected: it has 16 input channels. Using two of these ADC it is possible to acquire up to 32 channels, which can be strain gauges or other type of analog sensors.

The suggested component list with the cost estimation is reported in Table 2.3.

Component	Description	Quantity	Price [€]	Tot price [€]
wt12	Bluetooth module	1	21	21
stm32	microcontroller	1	2	2
lmt84	analog temperature sensor	5	0.5	2.5
ltc2418	16ch, 24 bit ADC	2	14	28
ina2322	instrumentation amplifier	11	3.3	36.3
sensors	strain gauge	22	10	220
bq24075	battery charger	1	2.6	2.6
res/cap	various resistor and capacitor	100	0.05	5
pcb	two layers - 75mm x 50mm	1	35	35
mikroe-1120	li-po battery - 2000mAh	1	14	14
			TOTAL	366.4
Dimensions				
Board	75mm x 50mm x 5mm (without programming header)			
Battery	63 mm x 44mm x 6mm			

Table 2.3: Suggested components of the proposed mobile system and their cost estimation.

As all wearable systems, the main problem of the proposed system is not related to electronics itself but rather to its integration on the boot. In fact, during skiing, impacts against soft and less soft snow can often occur and the wiring used in the in-door test is not suited to resist such events. Then the major effort has to be driven into shielding and protecting the sensors and the wires running around the boot.
Excluding any integration issues, we hypothesize at least 9 weeks of engineering work to develop a first portable prototype and a hardware cost of about 370 Euros (if manually assembled), as reported in Table 2.3.
All components should fit on a 70×50 mm^2 PCB, and we propose to pack the circuit and the battery inside a plastic case and fixing it on the boot toe, as we did for the socket board used during the experiments at LA SPORTIVA.

2.3 Infrared thermography

Infrared thermography can be used to measure temperature changes on the surface of materials due to stress generated thermal fields or externally applied thermal fields. Each body with a finite temperature emits an electromagnetic radiation from its surface, which is proportional to its intrinsic temperature. A part of this radiation is infrared radiation, which can be used to measure a body's temperature by means of the following equation:

$$T_{obj} = \sqrt[n]{\frac{U - CT_{amb}^n + C\varepsilon T_{amb}^n + CT_{pyr}^n}{C\varepsilon}} \tag{2.3}$$

where U is the detector signal, T_{obj} is the object temperature, T_{amb} is the temperature of the background radiation, T_{pyr} is the temperature of the device, ε is object emissivity, and C is the device specific constant. The parameter n is a parameter coming from a Taylor series expansion, being between 15 and 17 at wavelengths around 1 μm and decreasing up to $2-3$ at wavelengths around 14 μm [4].
Thermoelastic stress analysis (TSA), is a well-established non-contacting and non-destructive method that can provide stress data directly from the surface of a component. This method is based on the measurement of a small temperature change that occurs in a solid, when it undergoes to a cyclic load. It can be demonstrated that, in a linear, homogeneous and elastic material, the temperature change is directly related to the stresses according to following equation:

$$\Delta T = \frac{T}{\rho C_\varepsilon} \sum_{i,j=1}^{3} \frac{\partial \sigma_{ij}}{\partial T} \varepsilon_{ij} + \frac{Q}{\rho C_\varepsilon} \tag{2.4}$$

where T is the absolute temperature of the material, C_ε is the specific heat at constant strain, ρ is the material density, σ_{ij} is the stress change tensor, ε_{ij} is the strain change tensor, and Q is the heat input [5].
From here we can derive the basic first-order relationships between the stress change in an elastic solid and the resulting temperature change:

$$\Delta T = -KT(\sigma_1 + \sigma_2) \tag{2.5}$$

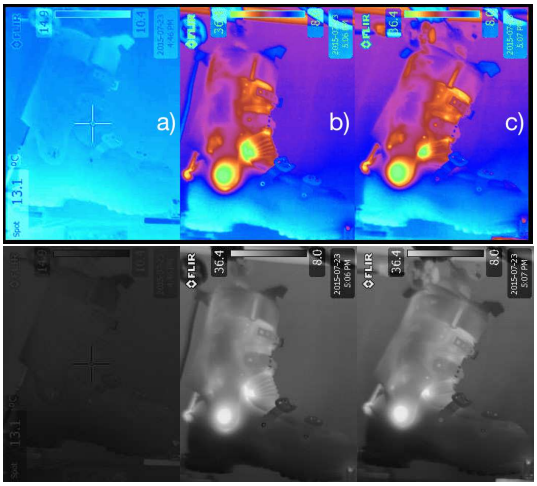

Figure 2.11: Infrared thermography acquired at a) initial state, b) after 600 cycles, c) after 600 cycles in stressed position. The low sensitivity of the FLIR camera mainly allowed the detection of frictions between the different components of the ski-boot

where K is the thermoelastic constant and $\sigma_1 + \sigma_2$ is the sum of the orthogonal direct stresses change on the surface of the solid [6, 7].

In order to detect temperature changes due to applied mechanical loads, a sensitive infrared camera with high response rate is needed. Common sensitivities reported in very first applications were 0.1 K although this sensitivity led to troubles with data measurements due to ambient conditions in many cases. Today sensitivities are in the range of 1 mK.

In our case, the available equipment was a FLIR 250 IR camera with a sensitivity of 80 mK at +30°C. The experiment was performed in the testing-chamber of the LA SPORTIVA's headquarter while the inner walls were covered with black cloths and in presence of no light source to reduce the ambient effect as much as possible. The ambient temperature has been set to 7°C, reproducing the actual usage condition of the boots.

It can be observed in Figure 2.11 that the main detected variation in temperature is in the moving parts which relates mainly to friction and the effect of stress on the fixed parts was not detectable due to insufficient sensitivity and response rate of the camera.

2.4 Photoelasticity measurement

The third approach used to investigate the stress distribution on the ski-boot is photoelasticity: an experimental method that allows the analysis of stress or strain fields on a sample. It is commonly used when analytical methods fail due to the complexity of the studied object or to the presence of discontinuities [8]. The physical phenomenon on which photoelastic studies are based is birefringence, that is the optical property of a material having a refractive index that

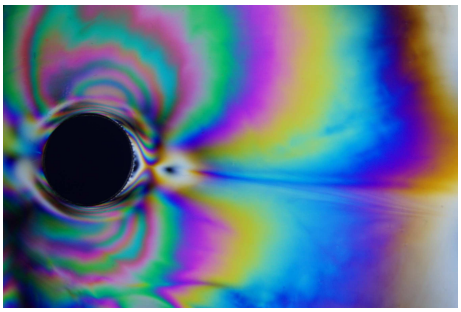

Figure 2.12: Residual stress in a polymer as visualized by photoelasticity.

depends on the polarization and propagation direction of light [9]. A ray of light incident upon a birefringent material is split by polarization into two rays taking slightly different paths. In particular, photoelastic materials are transparent non-crystalline and optically isotropic under normal (unloaded) conditions but become birefringent when stressed [10].
Photoelasticity can be experimentally visualized irradiating the sample with polarized light and observing the transmitted light through a polarizing filter. The stress in the material gives rise to fringes as can be seen in Figure 2.12. To better grasp the concepts behind the study of stresses by means of photoelasticity, we briefly discuss one of the experimental configurations that are commonly used: the plane polariscope [11, 12].

Figure 2.13 shows a transmission photoelasticity experiment. A beam of light (unpolarized, white or monochromatic) is directed through a polarizing filter placed between the light source and the sample (polarizing direction in the figure). As the beam of light enters the photoelastic material we can consider it as split in two components being polarized on two different directions (these directions depend on the stress directions within the sample) [13]. Since the material is birefringent, the two components experience different refractive indexes and therefore travel through the material at different velocities. As a result, at the moment of exiting the sample, one beam is retarded with respect to the other one. The light from the sample is then filtered by another polarizer, with axis perpendicular to the first one, so that only the components of the two beams having a polarization parallel to the second polarizer lattice are transmitted. The resulting beam results in two out-of-phase waves: the interference gives rise to the observed fringes.
It should be noted, however, that measurements taken with this particular setup are not always possible. In fact in many cases the sample to be studied does not consist of a photoelastic material. In such a case, two possibilities are usually considered for studying the stress distribution in the sample. One of them consists in reproducing a copy of the sample with a photoelastic material and study it in place of the actual sample. This approach involves some difficulties, such as production problems and the structural differences with respect to the original product.

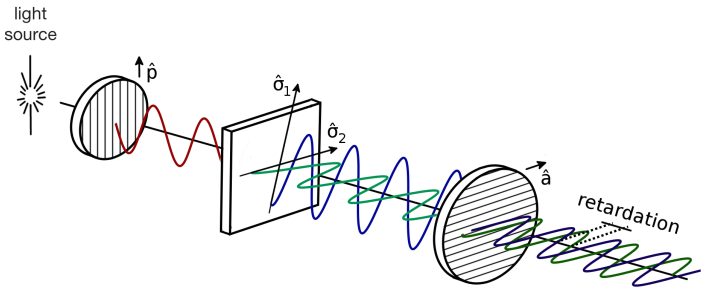

Figure 2.13: The plane polariscope. The two discs represent polarizing filters. The analysed sample is placed between them.

An alternative approach is reflection photoelasticity. In this configuration the sample is coated with a birefringent material and irradiated with polarized light. The reflected light is detected after being polarized again. If the coating has been deposited properly, when the sample is stressed the surface strains are transmitted to the photoelastic coating [12]. The main problem of this technique is the very low intensity of the reflected light, which is usually at least one order of magnitude lower compared to the intensities recorded in transmission photoelasticity [14].

Since our ski-boot is mostly made of a black and opaque (and therefore non reflective) polymer, we had to rely on reflection photoelasticity to study the stress distribution on it. To maximize the reflected light a part of the ski-boot was polished with an aluminium polishing machine and diamond paste and then a thin film (thickness of the order of few hundreds nm) of gold was deposited on it by sputtering. For practical reasons it was not possible to coat the whole boot with gold, so just a part of it was analyzed.
Epoxy resins are photoelastic [15], so we used a bicomponent glue (bisphenol-A and epichlorohydrin) as a photoelastic coating. A layer with thickness of approximately 1mm was deposited on the gold-coated sample and left 24 hrs at room temperature for curing.
We chose a white light source to obtain the signal as strong as possible. The light exiting the sample was filtered by a polarizer and then detected by a conventional camera. The obtained results are shown in Figure 2.14, where we can observe the clear difference between the relaxed and the stressed situation: the fringes can be easily observed in the right picture.
Clearly this is only a preliminary result to prove the validity of the technique and its applicability in non-ideal cases such as the study of an opaque and non reflecting surface. Many possible improvements would allow a better and more complete results and also quantitative measurements. First of all the study of the whole ski-boot could give a general overview of the stress field in the object. Qualitative analyses are easily obtainable but also quantitative measurements are possible once the characteristics of the photoelastic coating are known: specific products are available on the market and each of them has peculiar properties

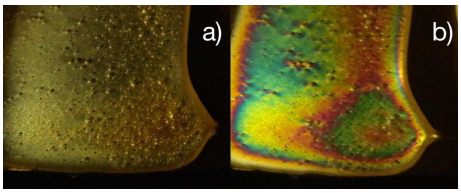

Figure 2.14: (a) Gold-coated PMMA sample covered by an epoxy resin layer. This particular covering makes possible to perform a reflection photoelasticity proof-of-concept.(b) Fringes observed on the studied sample when stressed.

that enhance the observation of stress fields on different materials in different situations.

To choose the proper photoelastic coating we have to consider different aspects: the method of application on the sample, the required sensitivity, the contour severity, the maximum elongation of the sample, the reinforcing effect and the test temperature. In particular, we are interested in the sensitivity which is the most important parameter if we want to perform quantitative analysis. We know that

$$\varepsilon_1 - \varepsilon_2 = \gamma_{max} = N\lambda/(2hK) = Nf \tag{2.6}$$

where ε_1 and ε_2 are the principal strains [μm/m], γ_{max} is the maximum shear strain [μm/m], N is the fringe order, λ the wavelength of the light, h the coating thickness, K the strain-optic coefficient of the photoelastic material [16]. The fringe value f represents the minimum difference in principal strains necessary to produce one fringe: the lower f, the more sensitive the coating.
Assuming the number of fringes to be observed (depending on the test condition and on the used instrumentation) and estimating the expected strain level the fringe value is calculated as:

$$f = (\varepsilon_1 - \varepsilon_2)/N = \mathcal{ES}/\mathcal{NF} \tag{2.7}$$

being $\mathcal{ES}$ the expected strain level and $\mathcal{NF}$ the maximum number of fringes desired. Once that f is calculated, the proper coating can be easily chosen [16]. Since f depends on the wavelength it could be useful to choose a monochromatic light source to perform quantitative measurements.

2.5 Conclusions

During the IPSP week our team suggested three possible solutions to the problem introduced by the company LA SPORTIVA.
First of all, we proposed a ski-boot sensorization by using strain gauges, through which it is possible to convert a mechanical stress into an electrical signal. We placed the stress sensors in different points on the boot. Then we set the application areas by means of know-how of the engineers of the company. This way it has been possible to draw a stress map of the boot during the tests, revealing the tendon region being the one most stressed part during the usage. This solution

allows an on-line measurement reducing dramatically the time needed for testing a single boot. It is possible to achieve quantitative information about the specimen robustness in real time without waiting for a whole breaking time. Furthermore, this solution enables to realize a database of stress maps for different boots, and in turn allows relating the building parameters (materials, geometries, etc.) to the final performance of the products.
We also led a feasibility study on the boot sensorization for outdoor tests. Through kind of a sensorization it is possible to measure the stress felt by ski-boot during the real skiing activity. Such a measurement is of course more trusty with respect to the one obtained during the tests on benchmark, and allows for a better investigation of the points where the boot is particularly sensitive to failure. Moreover, this could constitute the first step toward the calibration of the test chamber with appropriate pressure values.
Our team proposed also another solution to the LA SPORTIVA's issue, based on the study of the photoelasticity of certain materials when they are subjected to stress. During the week we proposed a proof-of-concept showing that this phenomenon can be exploited to realize a stress map of the whole ski-boot. A piece of the boot hull has been gold-coated and covered with a particular photoelastic resin. So, it has been shown how the photoelastic effect can be useful to detect any type of stress applied to the sample. Once that all of the boot would be treated, the measurements can give an immediate representation of the boot areas that are subjected to the greatest stress.
The techniques just described can be, in the end, applied simultaneously for qualifying, in a very precise way, the ski-boot designs. In our view, the two measures could be well accompanied: a first photoelastic analysis allows to realize a whole boot map highlighting the points that are more stressed during the skiing, while the second step consists in fixing the strain gauges in the critical points, in order to reach a precise measurement of stress values.
Thermography was also attempted but we faced up two main problems, which are the cost of high performance instrumentation and the unavoidable thermal noise caused by the the friction among the components of the ski-boot. Therefore this technique is not particularly appealing for this kind of application.
All the approaches described so far can represent the basis on which to build a FEM simulation, calibrated by the values collected during the experimental session. This would definitely enable the virtual prototyping, resulting in a great improvement within the R&D department of LA SPORTIVA.

BIBLIOGRAPHY

[1] K. Ueda and A. Umeda, "Dynamic response of strain gages up to 300 kHz," Experimental Mechanics, Vol. 38 n. 2, pp 93-98 (1998)

[2] `http://goo.gl/neICQl`

[3] `https://en.wikipedia.org/wiki/Wheatstone_bridge`

[4] Basic Principles of Non-Contact Temperature Measurement, `www.optris.com/downloads-infrared-cameras`

[5] Stanley, P. and Chan, W. K., "Quantitative stress analysis by means of the thermoelastic effect," Journal of Strain Analysis, n. 20, pp 129138 (1985)

[6] Dulieu-Barton, J. M. and Stanley, P., "Application of theromoelastic stress analysis to composite materials," sec. Strain, Vol. 35, n. 2, pp 41-48 (May 1999)

[7] Dulieu-Barton and J. M. and Stanley, P., "Development and applications of thermoelastic stress analysis," Journal of Strain Analysis, Vol. 33, pp 93-104 (1998)

[8] Proulx, T., "Experimental and Applied Mechanics, Volume 6: Proceedings of the 2010 Annual Conference on Experimental and Applied Mechanics," Springer Science end Business Media (2011)

[9] Bahaa E. A. Saleh and Malvin Carl Teich, "Fundamentals of Photonics," Vol. 81, Wiley Series in Pure and Applied Optics (2013)

[10] Sciammarella, C.A. and Sciammarella, F.M., "Experimental Mechanics of Solids," John Wiley and Sons (2012)

[11] Razumovsky, I., A., "Interference-optical Methods of Solid Mechanics," Springer Science and Business Media (2011)

[12] Ramesh, K., "Digital Photoelasticity," Springer (2000)

[13] Fang, L., "Study of Stress Measurement Using Polariscope," PhD thesis, Georgia Institute of Technology (2010)

[14] Sharpe, W.N., "Handbook of Experimental Solid Mechanics," Springer Science & Business Media (2008)

[15] Heywood, R.B., "Photoelasticity for Designers," Elsevier (2013)

[16] Micro-Measurements, "How to select photoelastic coatings," Tech Note TN-704-2 www.vishaypg.com

CHAPTER
THREE

INDUSTRIAL TORQUE SENSOR

M. Bernard, A. Calabrese , T. Chalyan, Z. El Koura, F. Dallari, S. Donadello, N. Gatti, T. Klaser, M. Leonardi, V. Regazzoni, A. Sartori

3.1 Introduction

3.1.1 The company

Founded in 1926, PAMA realizes industrial boring and milling machines and machining centers. The company has made a strong name throughout the world thanks to a combination of tradition and the technological excellence of its products, being an established supplier for a wide range of sectors as energy, heavy machinery and manufacturing, earthmoving, railway, aerospace, shipyard, machine tools and large diesel engine industries. All main structures are machined in-house, using PAMA boring-milling machines and machining centers with a defined, planned and continuously optimized industrial processes within the framework of a project of constant process and quality improvement. PAMA currently operates on the main markets in Europe, America and Asia; these facilities ensure direct sales support and prompt technical service with local personnel. In the local facility of Rovereto (Tn, Italy), an R&D center is present.

3.1.2 The problem

The company main asset is the production of boring-milling machines and machining centers. During the processing of raw metal workpieces, the machine may encounter irregularities in the amount of stock allowances, that lead to variations in the applied torque. Moreover, the "chatter" phenomenon may occur: the cutter enters a regime of oscillation spoiling the boring and possibly leading to breakage. An image of a spoiled bar and of the simulated cutting force behavior provided by the company, is shown in Figure 3.1. For the time being, a manual control is carried out by an operator inspecting the boring-milling process and controlling the rotation speed of the engine.

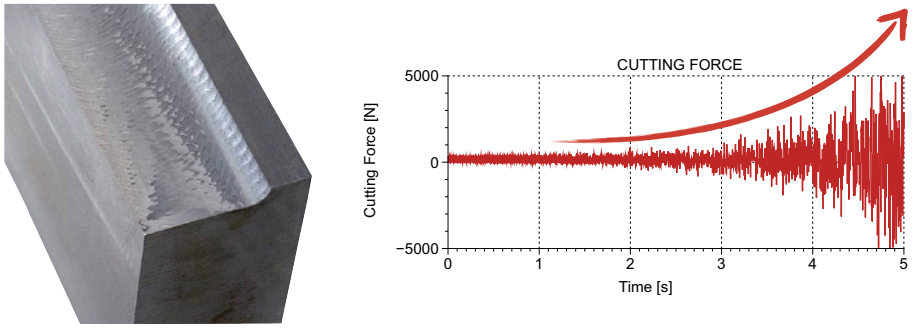

Figure 3.1: Effects of chattering on a metal bar and exponential cutting force noise growth leading to chattering.

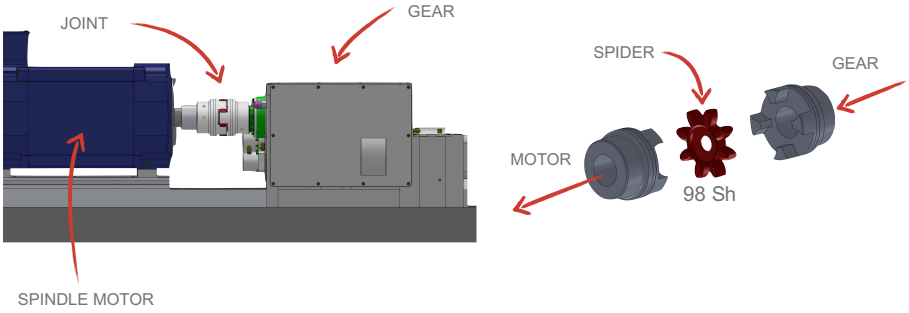

Figure 3.2: Coupling joint system and involved mechanical components.

The company wishes to automate the process, with the implementation of a sensor system capable of measure torque applied on the spindle, that is believed to be the critical parameter to oversee. The company suggests that the ideal point to measure the torque is the joint between the spindle motor and the gearbox, that is sketched in Figure 3.2. The joint includes an hard rubber spider to face small misalignments, which undergoes a deformation under the effect of the torque. The underlying idea is to measure the small deformation of the spider due to his elastic behavior and determine the torque using the elastic coefficient and/or a calibration curve. A sample joint was provided to the team by the company. The company therefore requests an on-board torque sensor for their machines, which should meet the following requirements:

- **Robust:** to endure industrial environment;
- **Easy to use:** it should not require specialized personnel to mount and use and should tolerate misalignments;
- **Economic:** budget is 300€;
- **Precise:** 5% full-scale;

Joint ROTEX GS65		Spindle Motor ROTEX 1PH8186		
Elasticity [Nm/rad]	Radius [mm]	Rotation [rpm]	Power [kW]	Max. Torque [Nm]
48520	67.5	5000	93	592

Table 3.1: Characteristics of the investigated mechanical system.

- **Versatile:** must measure in the wide range of process conditions.

Commercial solutions matching these specifications are available on the market, but at a price which goes well above the budget. The team is requested to conceive and possibly demonstrate a solution meeting all the above criteria.

3.1.3 System Description

Coupling joints are characterized by small dimensions, low weight and low mass moments of inertia despite the high torque transmission capability. Their application is ideal for transmitting torque while damping torsional vibrations and absorbing shocks produced by the uneven operation of certain prime movers. The two congruent coupling halves with concave claws on the inside are peripherally offset in relation to one another by half a pitch. In addition, they are designed in such a way as to enable an involute spider, typically made of polymeric material, to be located between them (see Figure 3.2). The teeth of the spider are crowned to avoid edge pressure if the shafts are slightly misaligned. This way, couplings are capable of compensating for small axial, radial and angular displacements of the shafts to be connected, which are always present. The spider in use on the examined machine is made of an improved polyurethane material, is resistant to high temperatures and has a long service life. As reported in Table 3.1 an important feature of the plastic gear connecting the motor and the gearbox is its elasticity: the spider is continuously subjected to compression as a function of the torque exerted by the working burr. The torque measurement is therefore deferred into an angular displacement measurement between the two claws of the joint, thanks to the spider's compressibility. The required features of the torque sensor, transposed in angular displacement using the nominal elasticity value, translate into a full-scale of 12.2 mrad implying a sensitivity requirement of 0.61 mrad. Table 3.2 compares the requirements of resolution and measurement range considering different possible approaches.

3.1.4 Suggested Solution

For the problem PAMA foresaw the following solution based on a magnetic circuit: a magnetic circuit, powered by and external inductance, measures the variations of magnetic current between a couple of interdigitated ferro-magnetic structures on the two sides of the joint, as sketched inf Figure 3.3.

Sensitivity	Angular [mrad]	Temporal [μsec] (5000 rpm)	Linear [μm] ($R = 67.5$mm)
Full-scale	12.2	23.3	823.5
Resolution	0.61	1.16	41.2

Table 3.2: Sensitivity and full-scale requirements for the sensor. The torque is converted into an angle using the nominal elasticity of the spider, in microseconds considering the maximum speed and in linear displacement considering the external radius of the joint.

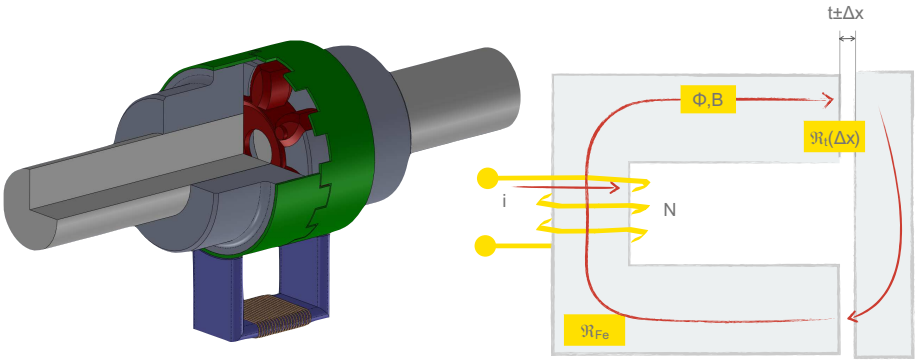

Figure 3.3: Magnetic circuit proposed by the company. The displacement of the ferro-magnetic elements (green interdigitated gears in the left panel), change the flux of magnetic field concatenated with the solenoid (sketched on the right).

3.2 Investigated Solutions

Many commercially available instruments use strain gauges to monitor the strain directly on the spindle, converting it into a torque. This kind of solution requires a power supply in the rotating system, an therefore makes use of sliding contacts or dedicated electronics. The company had already considered this option, that was discarded because of the unacceptably high cost. A research on the market and on the techniques used in scientific research to perform such measurements was then performed. From this preliminary research, the following list of possible solutions emerged:

- Piezoelectric crystal;
- LVDT (incorporates the suggested solution);
- Phase Sensitive Chopper.

In the following, these possible solutions will be briefly described, enlightening advantages and disadvantages for each.

Size	Spider Shore-GS	Shore range	Max. speed [rpm] for hub design					Torque [Nm]		Static torsion spring stiffness [1] [Nm/rad]	Dynamic torsion spring stiffness [1] [Nm/rad]	Radial spring stiffness C_r [N/mm]	Weight [kg]		Mass moment of inertia J [kgm²]	
			2.0 / 2.1 2.5 / 2.6	2.8 2.9	1.0 1.1	6.0 light [3]	6.0 P [3]	T_{KN}	$T_{K\,max}$				Each hub [5]	Spider	Each hub [5]	Spider
65	95	A	3800		3500	5650 [4]	11000	940	1880	48520	71660	6418	6,7	0,2	15143 x 10⁻⁶	437 x 10⁻⁶
	64	D						1175	2350	118510	189189	8670				
	72 [2]	D						1527	3054	160000	310000	11826				

Table 3.3: Extract of KTR company catalogue 2014 (pag. 148). The used spider model is GS65-95.

3.2.1 Piezoelectric

The torque measurement, as said, can be related to a displacement measurement at a fixed radius. Several methods can be used to perform this measure (i.e. capacitive, magnetic, piezo, etc.). In this section the piezoelectric ceramic transducer (PZT) solution is exploited. A piezoelectric is a material (typically a crystal) that accumulates electrical potential on his facets when put under strain. The easiest way to perform this measurement is therefore to place PZTs between the teeth, but this would require to modify the existing joint. Another possibility is to realize a crown gear, a "mask", around the joint were to put the PZTs.

Mechanics

From the point of view of a piezoelectric, the joint can be seen as a spring. Better to say, the spider inside the joint can be schematized as a parallel of eight springs. The spring stiffness of the spider from the KTR company is reported in Table 3.3. Having a stiffness k_{PZT}, a PZT is also a spring, so it should be added in parallel with the spring constant of the spider k_j. To protect the sensor from damages and to preserve the mechanical characteristics of the joint, the PZT is placed in series to another shunt spring k_S (see Figure 3.4) and the PZT with shunt spring system is placed in parallel to the effective spring of the joint's spider. The overall spring constant of the system can be calculated as:

$$k_{tot} = k_j + \frac{k_S \; k_{PZT}}{k_S + k_{PZT}}, \tag{3.1}$$

To preserve the mechanical characteristics of the joint, the spring constant of the series between k_S and k_{PZT} needs to be small compared to k_j. This situation can be achieved having $k_{PZT} \gg k_S$ and $k_j \gg k_S$. In such a case $k_{tot} \approx k_j$ and $\Delta x_{PZT} \approx \Delta x \; k_S/k_{PZT}$.

Implementation example

Lets analyze the case of the GS65-95 joint. For this component $k_j = 6418$ N/mm. A typical commercial PZT from PI Ceramic GmbH: P-883.31 that has $k_{PZT} = 24$ kN/mm, max travel range 11 μm and transduction constant 9.1 V/μm is chosen as an example. The shunt spring component is a parallelepiped of material with the appropriate dimensions and Youngs modulus to have $k_S \approx 600$ N/mm. The spring constant of this component can be calculated as $k_S = YA/L$ where Y is the Youngs modulus of the material, A is the area of the side and L is the length of

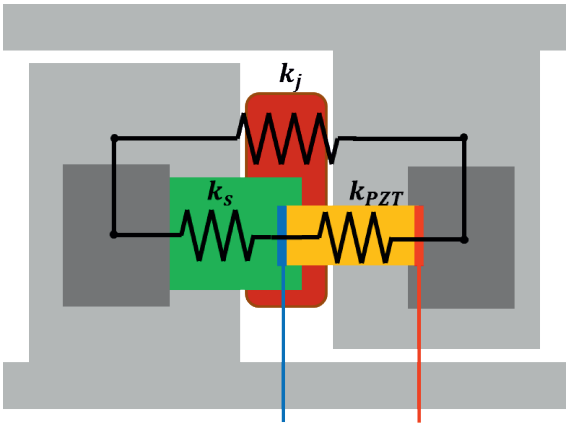

Figure 3.4: Piezoelectric ceramic (orange) fixed to the elastic support component (green) is mounted on the two parts of the joint (gray). The red and blue lines represent wires used to probe the potential on the PZT faces. The overlaying black lines represent a lumped element scheme of the system, where k_j is the spring stiffness of the joint's spider (central red block), k_{PZT} of the piezoelectric and k_s of the effective spring in series with the PZT.

Quantity	Units	Value
k_j	[N/mm]	6418
k_{PZT}	[N/mm]	24000
k_s	[N/mm]	360
k_{tot}	[N/mm]	6773
Δx_{PZT}^{max}	[μm]	12.35
Δx_{PZT}^{min}	[μm]	0.62
Trasd. constant	[V/μm]	9.1
V_{max}	[V]	112.0
V_{res}	[V]	5.6

Table 3.4: Mechanical properties of the overall system.

the parallelepiped. Choosing for example a 3mm $\times$3mm$\times$10mm parallelepiped of Teflon , $k_S = 360$N/mm. Knowing the spring constants of the three components, the overall quantities can be calculated. Results are reported in Table 3.4, while a proposed mounting scheme is shown in Figure 3.4.

Electronics

From the electrical point of view, a PZT is a series of a capacitor C with a voltage generator. To extract the signal from the rotating joint, one possible solution is to realize a capacitive circuit where one plate of the capacitor is on the rotating frame and the other is on the fixed frame. Since the joint can vibrate, the distance (d in the following equation) between the two capacitor plates can change and

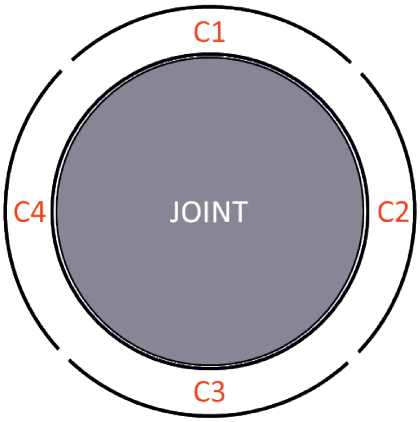

Figure 3.5: Scheme of the capacitive readout of the PZT. In this figure the vibration "isolation" is vastly exaggerated.

this change can mimic a variation of torque.

$$C = \epsilon_0 \epsilon_r S/d \tag{3.2}$$

As depicted in Figure 3.5, being the capacitive readout the parallel between C1, C2, C3 and C4, the system is at first order immune to vibration of the joint, as long as the vibrations are small compared to the distance between the capacitor plates. To explain how this part of the system works lets consider a vertical vibration of the joint. In such a case, C2 and C4 dont change, while C1 and C3 do. The total capacitance can be written as

$$C_{total} = \epsilon_0 \epsilon_r S \left(\frac{1}{d + \Delta x} + \frac{1}{d - \Delta x} \right) \tag{3.3}$$

where Δx is the distance change due to the vibration of the joint. If this variation is small compared to the total distance d, the small corrections Δx cancel each other at first order, leaving the total capacitance unchanged. In Figure 3.6 the capacitors C_t and C_r are the capacitor parallel explained in the previous paragraph. The top plates of C_t and C_r and the PZT are on the rotating system, while the bottom plate of C_t and C_r and the charge amplifier are on the fixed frame. The charge amplifier scheme is shown in Figure 3.6 (b). With this device the characteristic time of the system does not depend on the capacitor that needs to be measured but depends only from the feedback resistance and capacitor $\tau = R_f C_f$. In the end, the PZT creates a potential on a capacitor, which is transduced as a charge, which is then amplified and converted into a readout tension through the charge amplifier. The detection chain can therefore be summarized as:

$$V_{PZT} \rightarrow Q = V_{PZT} \left(\frac{1}{C_{PZT}} + \frac{1}{C_r} + \frac{1}{C_t} \right) \rightarrow V_r = -\frac{Q}{C_f} \tag{3.4}$$

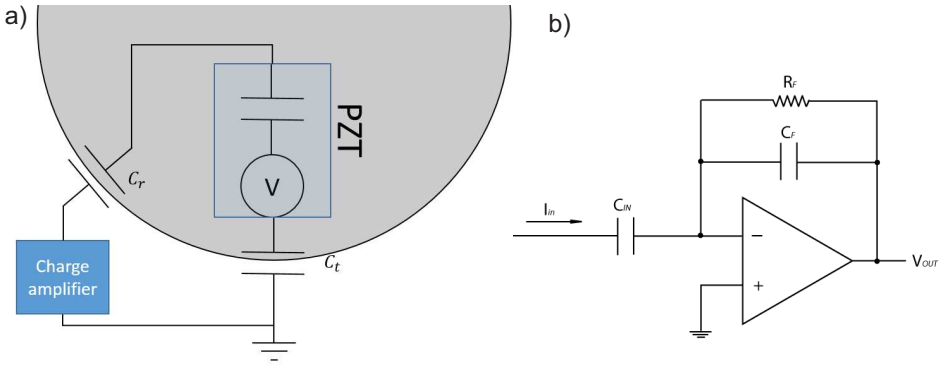

Figure 3.6: Electrical scheme of the piezoelectric readout system (a) and of the charge amplifier (b).

To have a stable and clean torque measurement, C_f must be as small as possible, but the product $\tau = R_f C_f$ must remain high enough compared to the sampling time.

Possible Issues

A PZT used in the so called "open loop configuration" presents two possible issues that may limit the resolution of the system. The first problem is the hysteresis. Open-loop piezo actuators exhibit hysteresis in their dielectric and electromagnetic large-signal behavior. Hysteresis is based on crystalline polarization effects and molecular effects within the piezoelectric material. The amount of hysteresis increases with increasing voltage (field strength) applied to the actuator. The "gap" in the voltage/displacement curve (see Figure 3.7 (a)) typically is around 2 %. The second problem is the so called creep/drift. The same material properties responsible for hysteresis also cause creep or drift. Creep is a change in displacement with time without any accompanying change in the control voltage. If the operating voltage of a piezo actuator is changed, the remnant polarization (piezo gain) continues to change, manifesting itself in a slow change of position. The rate of creep decreases logarithmically with time (see Figure 3.7 (b)). The capacitors used to drive the signal outside the rotating frame are sensitive to pollution and dust. A way to avoid this problem is to fill the gap between the two capacitors plate with a material. This solution would also increase the capacitance of the capacitors chain, improving the performance of the system, but it's not always easily achievable.

3.2.2 LVDT

While investigating the magnetic circuit solution that was initially proposed by the company, a system of two coupled inductive circuits was hypothesized. In this configuration, the area that concatenates the two arms of the circuit is varied by the small deformation of the spider, producing a variation in magnetic flux.

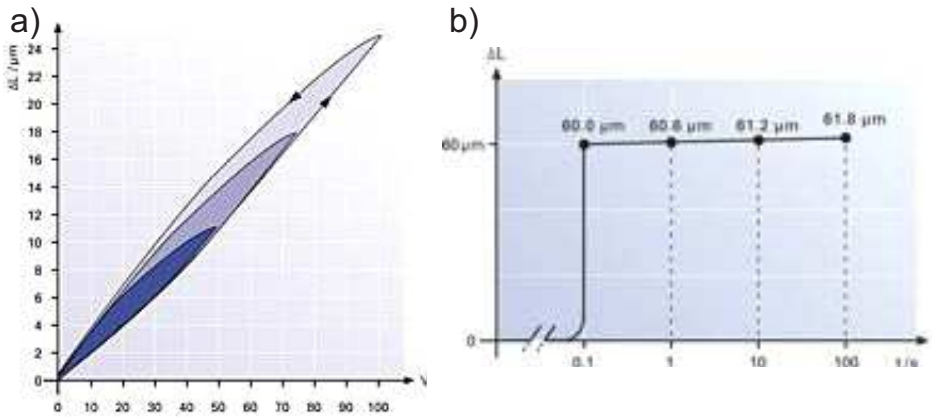

Figure 3.7: (a) Hysteresis curves of an open-loop piezo actuator for various peak voltages. The hysteresis is related to the distance moved, not to the nominal travel range.(b) Creep of an open-loop PZT motion after a 60 μm change in length as a function of time. Creep is on the order of 1% of the last commanded motion per time decade.

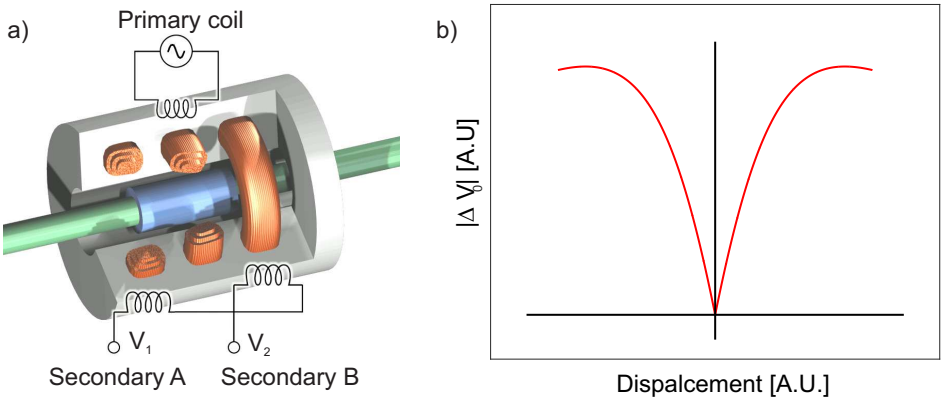

Figure 3.8: (a) Scheme of a LVDT [3]: a ferromagnetic core (blue) anchored to a handle (green) unbalances the three coil system embedded in the shiel (gray).(b) Typical differential output voltage modulus of an LVDT as a function of displacement. The response is linear for small displacement [4].

A commercial solution exploiting a similar concept is already available under the name of Linear Variable Differential Transformer (LVDT). LVDT systems meeting the sensitivity requirements are commercially available at around 150€, plus the cost of the dedicated electronics. The critical points of this class of solutions are the sensitivity to vibrations that add noise to the measurement and the necessity of implementation of electronics on the rotating joint. Since LTDVs are already commercialized and characteristics vary greatly among different models, a market research was performed, finding overall implementation slightly above the 300€ threshold with models that should be tested for stability in the dynamic conditions [2]. As shown in Figure 3.8 an LVDT is composed by:

- a Primary coil;
- two Secondary coils A and B;
- a ferromagnetic core;
- a shield;
- an handle.

The ferromagnetic core is the moving component whose position within the shaft is sensed. The three inductors are wound around the shaft: the primary winding (Primary coil) in the middle and the secondary windings (Secondary coils A and B) on either side of the primary. Each of the secondary coils should have the same number of turns and be of the same length, so that at the null position (when the core is centered on the primary coil) the system is balanced and can be approximated as linearly with respect to displacement. A cylindrical shield protects the windings from damage and also serves to contain the magnetic field used for sensing. The physical component which will be measured using the LVDT is mechanically coupled to the ferromagnetic core using a non-ferromagnetic handle.

Physical principle

When the primary coil is excited with a sine wave voltage, it generates a variable magnetic field that, concentrated with the core, induces the secondary voltages (also sine waves, as shown in Figure 3.9 [5, 6, 7]). While the secondary windings are designed so that the differential output voltage ($\Delta V_0 = V_1 - V_2$) is proportional to the core position from the null position, the phase angle (close to 0 or close to π, depending on the direction) determines the direction away from the mechanical zero.

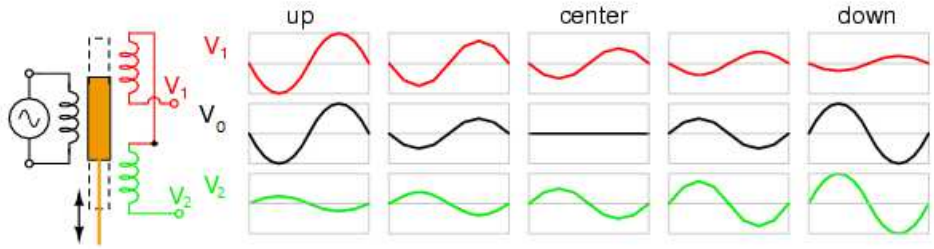

Figure 3.9: A set of two inductive circuits are arranged as shown in Figure 3.8. A ferromagnetic core is placed inside the primary circuit (left). In this configuration the coils of the secondary circuit (right) are aligned in such a way that, in equilibrium condition, no current is transferred between the primary and the secondary circuit. If a little displacement occurs, changing the ferromagnetic core position, the secondary circuit will be no longer balanced and a current will start to flow between V_1 and V_2.

Figure 3.10: A classical chopper, used to test the response of the used laser diode and photodetector.

Advantages and drawbacks

The LVDT has many advantages: being a mature technology, robust and reliable sensors with a good linearity are available on the market. Since they are used for a range of applications, it should be possible to find a device with the required resolution and specifications (resistance to the industrial environment, vibrations, acceleration) although the cost may vary greatly. There are, however, some drawbacks worth noting: the driving circuit plays a crucial role in the instrument performance, and it should be placed on the joint along with the sensor. Furthermore, the sensor and his driving circuit have to be powered by an external source and require a system to deliver the data.

3.2.3 Chopper

The optical chopper is a widely used instrument in physics research. The chopper concept is simple: a light beam is periodically interrupted (chopped) by a regularly perforated disk, connected to a rotating axis. When the axis rotates, disk and holes modulate the light beam. A detector collects the modulated light, producing a signal whose frequency is proportional to the rotation speed of the axis, and the phase is locked with the disk holes. In Figure 3.10 a classical chopper is shown. The fact that both frequency and phase may be measured by an optical chopper allowed the realization of locked-in-phase amplifiers, a nowadays omnipresent instrument in any experimental laboratory. As mentioned above, the problem of measuring the torque may be translated, thanks to elasticity, into the measurement of an angle between the two arms of the joint, which is basically an angular phase. Therefore, a system measuring the relative phase among two choppers mounted on the two arms of the joint can be considered.

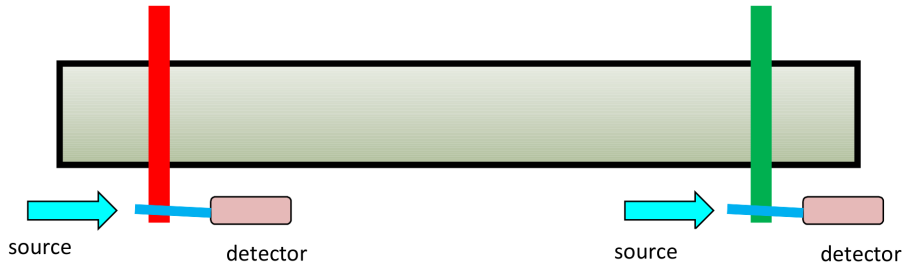

Figure 3.11: Typical double-chopper configuration.

Possible implementation

We found that this technique is already used to measure the torque applied at long bars, basically using two complete choppers and measuring the relative phase among them [8]. Two metal or hard plastic bladed masks, mounted on the two sides, act as modulators. A laser diode's beam of light is shined through each mask and is detected by a couple of photodetectors placed on the other side, as shown in Figure 3.11. The phase between the two choppers may be easily compared with simple electronics, giving a direct measure of the angular shift due to the spider compression. The main advantages of the chopper technique are the extremely low cost, reliability and immunity to electromagnetic noise. The last two in particular are due to the fast data acquisition at regime, which may be used for averaging, and the nature of the output signal: a single TTL. Furthermore, having a TTL output signal allows makes the digitalization and calibration process easy to be performed directly on board. The main drawback is the requirement of a relatively clean environment, where the laser diode and the photodetector may work. While this problem could in principle solved by insulating the optical part in a box (but that is not well seen by the company, because of cost and required space), a more elegant solution was foresee using magnets and hall sensors. Therefore, it was decided to develop the chopper idea in both its configurations, realizing a demonstrator for both. The design and demonstration of both the chopper configurations is detailed below.

3.3 Phase sensitive chopper

After the analysis of the possible solutions, the phase sensitive proposal appeared to be the most promising. Therefore, the group reworked the design and possible implementation of this solution adapting it to the specifics of the problem, also realizing a demonstrator. Since it was discovered that a similar implementation (optical encoder) was already being used in the past by the company but was then abandoned, an alternative approach that makes a synthesis of the precision, reliability and low cost of the phase sensitive chopper with the dirt-environment immunity of a magnetic circuit was also implemented. These two solutions (optical and magnetic chopper) have many parts in common, an may be realized at the

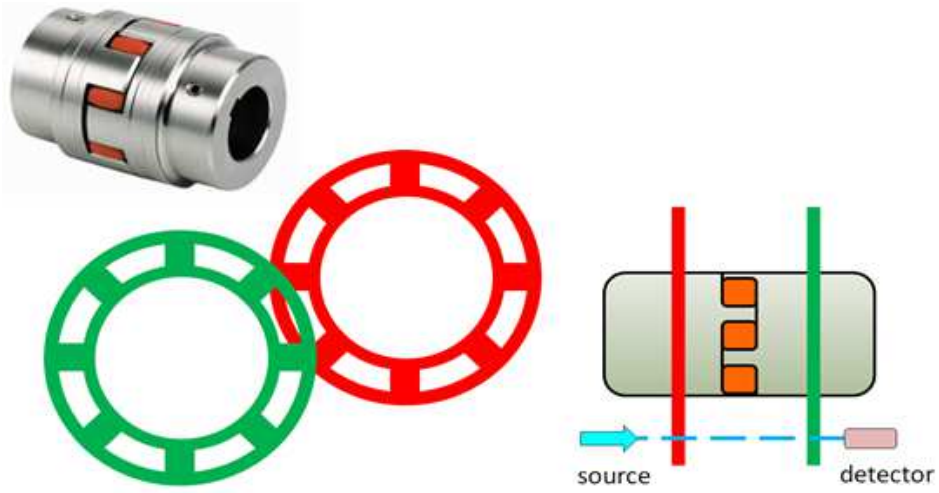

Figure 3.12: Optical chopper configuration on the joint.

Figure 3.13: Relative dephasing of the bladed wheels varies the aperture and therefore the duty cycle of the optical signal, maintaining the same frequency.

same time well within the budget, increasing the robustness of the measure.

3.3.1 Optical chopper

The proposed solution in comparison with already used commercial solutions has few valuable advantages. The system shown in Figure 3.11 uses two couples of light sources and photodetectors, because the two choppers are required to be at a distance to exploit the elasticity of the bar itself. In Figure 3.12 we propose a cheaper and easier solution, that is more compact and more robust. In this case, a single laser diode-photodetector pair is used to measure the modulation of a single laser beam that crosses both masks. The masks should be mounted such that when no torque is applied, the blades of on the two arms are dephased of half a period. In this way, additional change in the phase of the two masks linearly varies the duty cycle of the signal(see Figs. 3.13 and 3.14). In the end, the speed of rotation and the torque are obtained from the measurement of the frequency and duty cycle of the photodetector signal respectively by standard electronics.

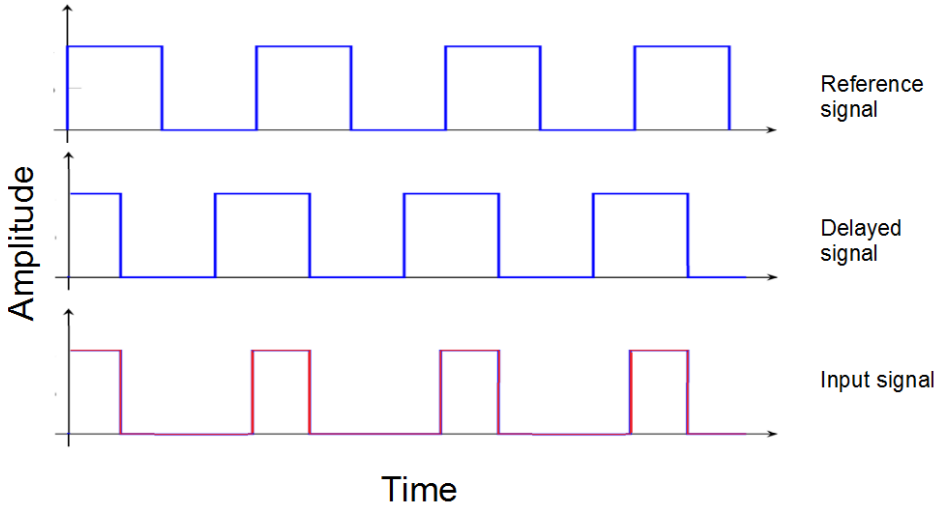

Figure 3.14: Phase shift due to relative misalignment of the two choppers. The rotation speed and the torque are obtained from the measurement of the frequency and duty cycle respectively.

3.3.2 Experimental scheme

A demonstrator of the solution was designed and realized during the event week in the laboratories of the Department of Physics. The experimental setup features a profiled aluminum disk mounted on an electric motor, as shown in Figure 3.15. As a laser source an Hermetic Infrared Emitting Diode OP130 Series was selected, while as photodetector an OPL800 was used. The choice on this components is really wide, and in this case was driven by the immediate availability in the Department's electronic warehouse. Other laser-photodetector pairs are available on the market, with different wavelengths and power ranges, allowing for a more robust measure even in dirty environment.

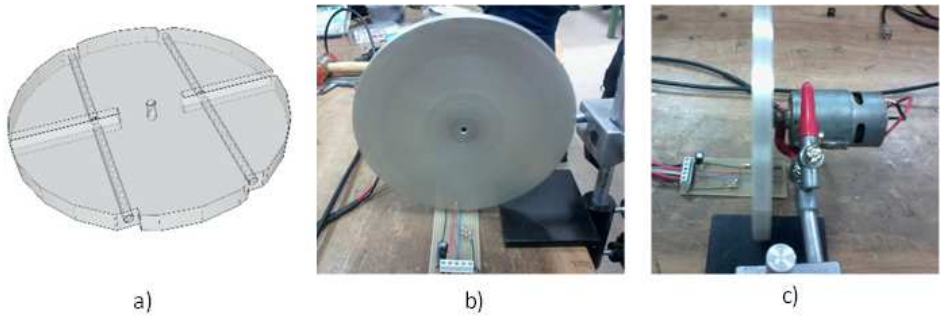

Figure 3.15: Final design of chopper. a) design and b),c) testing of the demonstrator.

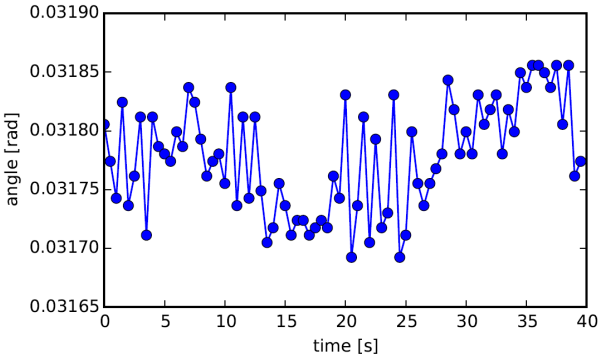

Figure 3.16: Sample data acquired during the testing phase, demonstrating the sub-milliradiant precision.

3.3.3 Results

The measurement system is based on a STM32F4 microcontroller characterized by low cost and high performances running the StdPheriphLib from STMicroelectronics. The signal source is the infrared photodiode, giving a TTL 0-5V square signal. The signal is acquired through a GPIO pin of the microcontroller that exploiting an embedded timer in PWM mode returns directly the duration of both high and low intervals of the square signal. From this, with elementary calculations performed on-board, the frequency and the duty cycle of the signal are obtained. These values are transmitted via USART serial communication to a PC software written in Python that shows the rotation velocity and the torque in real time. The frequency of the timer (84MHz) is more than enough for the required resolution of the measure and the 16bit counter is enough to provide correct sampling in the low rotation speed regime. A sample of the collected data is shown in Figure 3.16. For the realized system, sub-milliradiant was already achieved, despite the use of just two holes and of the rather unstable electric motor. In a definitive realization, the number and dimension of the blades has to be chosen carefully, based on the required resolution and the minimum-maximum rotation speed of the joint.

3.4 Dimensioning the system

From the information provided by the manufacturer the following parameters relating to the joint are known:

- it operates between 30-5000 rpm;
- the two components of the joint could have a maximum angular displacement of 12.2 mrad with torque application, as shown in Table 3.2.

In addition, an uncertainty below 5% of full scale was requested, implying a resolution of 0.61 mrad, with a sampling rate around 10Hz. From the previous

conditions, in order to have a sufficient sampling rate at low speed (30 rpm, or 0.5 Hz), a number of blades $N = 20$ is required. In order to benefit from averaging, $N = 100$ was considered instead, giving 50 samples per second. This number is compatible with the minimum blade-hole dimension required for the resolution, for which the opening is required to be larger than two times the total angular shift. With the proposed parameters, the with of each slit $w_s = 2\pi/2N = 31.4$ mrad $> 2 \times 12.2$ mrad $= 24.4$ mrad satisfying the resolution criterion. In conclusion we have found that the operative mask wheel should have 100 blades and holes of about 2mm each to meet the required resolution and exceed the low rotation speed sampling requirements.

3.4.1 Magnetic Chopper

The "magnetic chopper" measurement setup relies on the same operational principle at the core of the optical chopper setup, though exploiting a different physical phenomenon: the signal, detected by a hall sensor, is modulated by the presence of magnets with alternate polarization on the rotating wheel. While on one side this solution is slightly less immediate than the optical chopper, the use of magnetic field as a signal makes the system practically immune to the presence of dust and oil. It therefore promises to have the long-lasting reliability, which was one of the requisites we were asked for. The feasibility of this idea was tested experimentally: exploiting the limited time and resources, a demonstrator was realized, analogue to the optical chopper.

Demonstrator

A rotating wheel analogous to the one of the optical chopper was realized in plastic material (Figure 3.17). Four magnets were inserted in the wheel by drilling small holes. The number and strength of the magnets was set by the immediate availability.

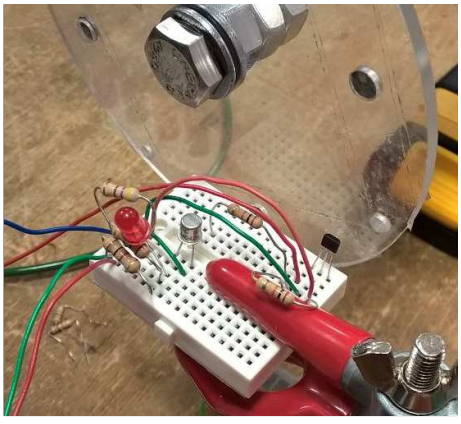

Figure 3.17: Demonstrator of the magnetic chopper. The hall sensor circuitry and the magnets on the wheel are visible.

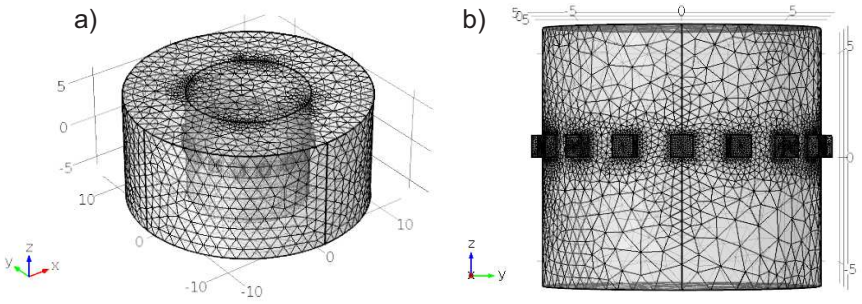

Figure 3.18: (a) Full simulation domain with the mesh. The inner cylinder represents the steel joint and the parallelepipeds on its surface are the magnets. The outer cylindrical shell is made of air and sets the limits of the simulation domain. (b) Front view of the geometry drawn to represent the joint, without the air shell. It is apparent how the mesh is set to be finer around the interested region.

FEM simulations

We also began to set a theoretical model of the device based on simulations. The reasons for this are manifold. Our experiment had mainly the aim of testing the Hall sensor, i.e. to see if it is able to work at the required frequency and measure its response time. There remain many parameters that may be optimized, giving space for much improvement, such as the material for the magnets and its magnetization density, the size, shape and spacing of the magnets on each chopper wheel, the spacing between the two wheels, the distance at which the sensor has to be placed, the maximum amount of magnetic noise tolerable in the apparatus, due for example to the electric engine or the presence of ferromagnetic dust. Simulations provide us a valuable tool to quantitatively estimate the dependence of the sensor operation on these parameters. Due to the limited amount of time, we were able to draw and simulate only a very simple system, but it was nevertheless useful and sufficient to get an idea of the quantities involved and realize a demonstrator. Moreover, the method is general and easily applicable to a more realistic system, once a proper experimental design is provided. The joint is modeled as a simple cylinder made of structural steel. On its surface, 16 small parallelepipeds are placed to represent the magnets and a larger cylinder made of air surrounds the structure (Figure 3.18). The simulation volume is divided in small domains with the help of a grid of small tetrahedra, the mesh, which is built by a proper algorithm in the software. Maxwell's equations are solved on the mesh grid, with the appropriate boundary conditions. As can be seen from Figure 3.18 (b), the mesh is finer in the domains corresponding to magnets and near the edges, where fields vary more rapidly. Initially, the spatial distribution of the magnetic induction field B, due to the presence of sources, characterized by a permanent magnetization density is determined. Therefore, Ampere's law has to be solved in the stationary case:

$$\nabla \times \mu_0^{-1}\mu_r^{-1}\left(B - B_r\right) - \sigma v \times B = J_e \tag{3.5}$$

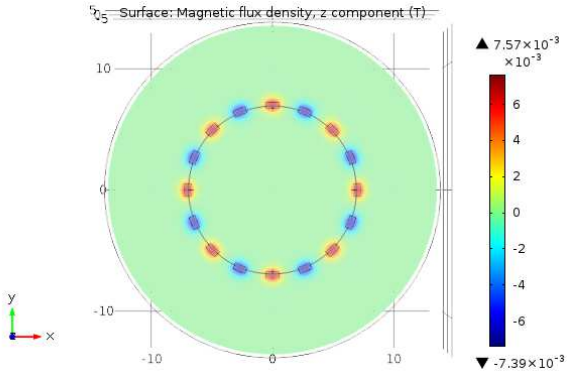

Figure 3.19: Top view of the studied geometry, showing how the presence of the magnets can be simulated by introducing a proper remnant flux density of magnetic induction field, B_r. Red parallelepipeds represent magnets with north pole up and south pole down (along z), while blue ones are oriented the opposite way. Br has zero components both along x and y.

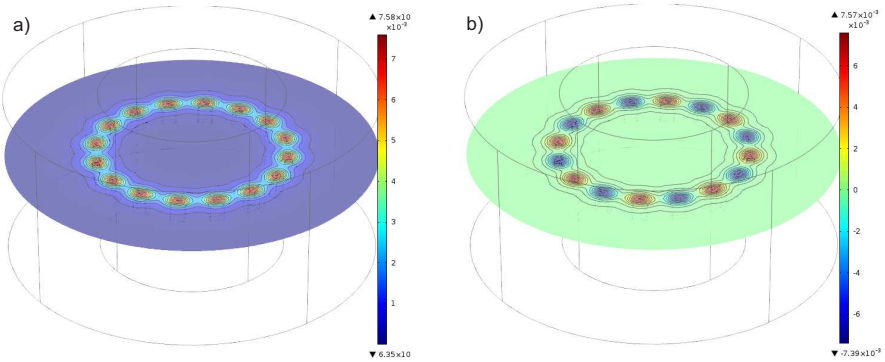

Figure 3.20: Results of the simulation, showing the total magnetic energy density $H \cdot B$ (a) and the magnetic flux density B_z (b) distribution along a plane, which is perpendicular to the cylinder axis and to the direction of the remnant flux density within the magnets. The B field distribution is reported both as a surface plot, showing the relative intensities, and as a contour plot, showing the field lines.

$$B = \nabla \times A \tag{3.6}$$

In the equation, J_e represents the total free current density, which is considered null. The second term on the left-hand side is instead the current due to free point charges, moving at velocity v in a medium of conductivity σ: this term is also considered null. B_r is called residual magnetization density and corresponds to the magnetic field produced by the magnets. μ_r is the relative magnetic permeability and is considered in first approximation as 1 everywhere. Also the magnets are here fictitiously set at unitary permeability, because they are completely characterized by the presence of the residual magnetization B_r. As is illustrated in Figure 3.19, the magnets can be divided in two groups with opposite orientation. The modulus of B_r is set for each magnet at the value of 810 G. This is

the value we measured with a Hall probe for the magnets we actually used in the experiment, but more powerful rare-earth magnets are nowadays available on the market at a low price. The boundary conditions chosen are that of magnetic insulation: the simulation domain is set to be isolated from any external source of magnetic field. This is made possible by imposing the condition $n \times A = 0$ on all the boundaries delimiting the geometry, with n the versor normal to each surface. This equation means that there is no net flux of magnetic field across the external boundaries, therefore the total flux within the simulation domain is conserved. Simulation results are shown in Figs.3.20 a) and b), for B_z and $|B|^2$ respectively. For the sake of clarity, results are computed along a cut plane perpendicular to the cylinder axis. Relative intensities of the fields are shown as well as field lines. As already stated, these results are preliminary. They, however, provide the basis for setting a more complete and detailed model, having in mind the design of a magnetic chopper having the proper number of "slits" and blades needed to achieve the required resolution. The Hall sensor must be able to follow the rotation of the two wheels in the given frequency range and to sense their required minimum displacement. Further steps to be taken into account can be:

- include the joint geometry and the magnetic permeability of the steel components;
- include two magnet wheels instead of one in the geometry and study the magnetic field distribution in this configuration;
- vary the magnets size and spacing searching for the maximum density. If it's not possible to have enough magnetic inversions per round trip, the radius of the wheel can be increased;
- make the system rotate and see how the fields evolve in time, at different rotation frequencies;
- look at the setup tolerance: what is the effect of displacing some magnets from their ideal position.

3.5 Conclusions

During the IPSP2015 our team faced the problem proposed by PAMA, up to the realization of a demonstrator for suggested solution. A first bibliographic research step was taken out. While direct torque measurement techniques were considered, the solutions exploiting the joint elasticity proved to be much more appealing within the time limit of the event. From the bibliographic research, three possible approaches to solve the problem stood out: the piezoelectric crystal, the LVDT and the phase sensitive Chopper. The advantages and drawbacks of each technique are summarized in Table 3.5. Consequently, the phase sensitive chopper was chosen as the most suitable solution. After some reworking it was decided to bring on both the optical and the magnetic chopper idea, as the solutions are very similar, and could be easily used together. In the case of the magnetic chopper, spare components were used, allowing to demonstrate the concept. A

Approach	Advantages	Drawbacks
Piezoelectric	Simple, cheap, linear	Capacitive reading, hysteresis, creep
LVDT	Well known, robust, linear, durable	Delicate driving circuit, electronics on joint
Chopper	Extremely cheap, fast, non invasive, simple system, simple electronics	Optic requires clean environment

Table 3.5: Advantages and drawbacks of the three possible solutions.

work of simulation to push the limits for the requirements in terms of number and strength of magnets required was then outlined. For the optical chopper, all the components were available in the Department's warehouse, permitting the realization of a complete demonstrator, meeting the resolution requirements, up to the acquisition board and software using very cheap components. The overall cost of the sensors and acquisition board stays well within 100€, leaving the rest for the realization of the ad-hoc mask on the joint, to host the blazes and/or the magnets wheel, meeting all the requirements.

BIBLIOGRAPHY

[1] A. Safari, V. F. Janas, A. Bandyopadhyay and A. Kholkine "Piezoelectric Transducers and Sensors". *The Measurement, Instrumentation and Sensors Handbook.* CRC Press, Boca Raton, 1999.

[2] LVDT on digikey.com `http://goo.gl/UBWLNZ`

[3] adapted from `https://commons.wikimedia.org/wiki/File:LVDT.eps`

[4] C. P. de Souza , M. B. Wanderley 16^{th} IMEKO TC4 Symposium

[5] LVDT on sensorwiki.org `http://goo.gl/us7IdA`

[6] Halit Eren, "Inductive Displacement Sensors". *The Measurement, Instrumentation and Sensors Handbook.* CRC Press, Boca Raton, 1999. Instrumentation and Sensors Handbook. CRC Press, Boca Raton, 1999.

[7] `http://www.lvdt.co.uk/how-lvdts-work/`

[8] Commercial chopper example: `http://goo.gl/yV1Qun`

CREDITS

COSTER Tecnologie Speciali TEAM

From left to right upper row: M. Fidanza[1], C. Bortignon[2], M. Campestrin[2] , A. Lugnan[2] , F. Rozio[2] ,A. Trenti[2] , M. Borghi[2] , L. Matordes[1] , A. Tecchiolli[1] , F. Deflorian[3]

From left to right lower row: M. Mancinelli[2] , S. Signorini[2] , M. Pelz[1] , G. Zendri[2] [4]

Not in figure: G. Bortolotti[2]

[1]COSTER Tecnologie Speciali S.p.a., Viale Trento 2, I-38050 Calceranica al lago, Trento, Italy
[2]Department of Physics, University of Trento, via Sommarive 14, I-38123 Povo, Trento, Italy
[3]Vice-rector, University of Trento, via Calepina 14, I-38122 Trento, Italy
[4]IPSP2015 scientific committee


INDUSTRIAL
PROBLEM SOLVING
WITH PHYSICS

LA SPORTIVA TEAM

From left to right: S. Amirabdollahian[1], M. Bertolla[2], C. Piotto[2] , D. Giovannelli[3], C. Castellan[2] , D. Roilo[2] , M. Azzolini[2] , M. Secchi[2 3] , S. Tondini[2 45], C. Nidasio[6]

Not in figure: L. Cossu[2] , E. Demenev[3]

[1]Department of Industrial Engineering, University of Trento, via Sommarive, 9, I-38123 Povo, Trento, Italy
[2]Department of Physics, University of Trento, via Sommarive 14, I-38123 Povo, Trento, Italy
[3]Bruno Kessler Foundation, via Sommarive 18, I-38123 Povo, Trento, Italy
[4]Dipartimento di Fisica, Informatica e Matematica, Universitá di Modena e Reggio Emilia, Via Campi 213/a, I-41125 Modena, Italy
[5]IPSP2015 scientific committee
[6]Research and Technology Transfer Support Division, University of Trento, via Calepina 14, I-38122 Trento, Italy


LA SPORTIVA
BER
LIN

PAMA TEAM

From left to right, upper row: A. Sartori[1], S. Donadello[1] , N. Gatti[1] , T. Klaser, M. Leonardi[1] , F. Dallari[1]

From left to right, lower row: T. Chalyan[1] , Z. El Koura[1] , V. Regazzoni[1 2], A. Calabrese[1] , M. Bernard[1 2 3]

[1]Department of Physics, University of Trento, via Sommarive 14, I-38123 Povo, Trento, Italy
[2]Bruno Kessler Foundation, via Sommarive 18, I-38123 Povo, Trento, Italy
[3]IPSP2015 scientific committee


PSP2015
datch
POWER INVERTER

ACKNOWLEDGEMENTS

We acknowledge the role of the Department of Physics, the Doctoral School in Physics, the Research and Technology Transfer Support division of the University of Trento, Confindustria Trento and Trentino Sviluppo - Polo della Meccatronica. In particular we would like to thank the people who personally cooperated, as members of the Advisory Board of IPSP2015, towards the success of this second edition: prof. Lorenzo Pavesi, prof. Giovanni Andrea Prodi, dott.ssa Vanessa Ravagni, dott. Alessandro Santini, dott. Paolo Gregori.
We are also grateful to dott. Claudio Nidasio and dott. Lino Giusti for the helpful aid in the field of intellectual property and relationship with the companies.
We are grateful to COSTER Tecnologie Speciali S.p.a., LA SPORTIVA S.p.a. and PAMA S.p.a. for the enthusiasm and the support they gave us during the IPSP2015 week, and to all the students/researchers that had been working hard during the event. We would like to thank the IPSP2015 sponsors: Dolomiti Energia, UTE MED s.r.l., Famiglia Cooperativa di Povo and Cassa Rurale Pinetana, Fornace e Seregnano for their financial support.
IPSP2015 could not have been organized without the help of the staff of Communication and events office - Polo Collina, of the Legal office and of the Graphic Service of the University of Trento. In particular we would like to express our special thanks to Lucia Dorna, who followed every step of this event with passion and professionalism. We are also proud to thank those who helped us in the promotion of this event, especially Alessandra Saletti and Elisabetta Andreina Brunelli (press office of University of Trento) and Davide Modena (press office of Trentino Sviluppo). We want to express our gratitude also to the staff of the Didactic Laboratories, Department of Physics of University of Trento, who made their instrumentation and laboratories available.
Finally a special thank goes to the IPSP2014 Scientific Committee, to our wives and girlfriends, and to all the people who supported us, in different ways, in the realization of the event Industrial Problem Solving with Physics, edition 2015.

ART>UNITRENTO
March 2016

IPSP2015, Industrial Problem Solving with Physics 2015, is a one-week event organized by the Department of Physics, the Doctoral Programme in Physics and the Research and Technology Transfer Support Division of the University of Trento, in collaboration with Confindustria Trento and Polo Meccatronica - Trentino Sviluppo.

3 companies and 30 brains (master students, PhD students and research fellows) were selected and worked together to find solutions to practical industrial problems proposed by the participating companies.

Young and motivated researchers had the chance to demonstrate their own skills in tackling new practical challenges. The participating companies obtained concrete solutions to the problems and experienced an alternative problem solving strategy.

http://events.unitn.it/en/ipsp2015

Participant companies

COSTER

LA SPORTIVA innovation with passion

PAMA

Sponsors

Dolomiti energia

CASSA RURALE PINETANA FORNACE E SEREGNANO BANCA DI CREDITO COOPERATIVO

coop Trentino

ISBN 978-88-8443-674-0